1 **High frequency, continuous measurements reveal strong diel and seasonal cycling of**
2 **pCO$_2$ and CO$_2$ flux in a mesohaline reach of the Chesapeake Bay**
3
4

5 **A. Whitman Miller[1*], Jim R. Muirhead[1], Amanda C. Reynolds[1], Mark S. Minton[1] and Karl**
6 **J. Klug[1]**

7 [1]Smithsonian Environmental Research Center, Edgewater, MD USA
8

9 Corresponding author: A. Whitman Miller (millerw@si.edu)

10 †Additional author notes should be indicated with symbols (current addresses, for example).

11 **Key Points:**

12 • Automated pCO$_2$ measurements capture daily cycles and anomalous events in estuaries
13   where pCO$_2$ changes rapidly and across a wide range.

14 • Rhode River is net autotrophic (Dec-May), net heterotrophic (Jun-Nov), NEP is near
15   balanced annually, but can reverse status during a single day.

16 • Year-round continuous measurements reveal that pCO$_2$ and CO$_2$ flux are mediated by
17   temperature effects on biological activity and are inverse to the physical solubility of
18   CO$_2$.
19
20

21 **ABSTRACT**

22 We estimated hourly air-water gas transfer velocities (k_{600}) for carbon dioxide in the Rhode

23 River, a mesohaline subestuary of the Chesapeake Bay. Gas transfer velocities were calculated

24 from estuary-specific parameterizations developed explicitly for shallow, microtidal estuaries in

25 the Mid-Atlantic region of the United States, using standardized wind speed measurements.

26 Combining the gas transfer velocity with continuous measurements of pCO$_2$ in the water and in

27 the overlying atmosphere, we determined the direction and magnitude of CO$_2$ flux at hourly

28 intervals across a 3 yr record (01 July 2018 to 01 July 2021). Continuous year-round

29 measurements enabled us to document strong seasonal cycling whereby the Rhode River is

30 primarily autotrophic during cold-water months (Dec–May), and largely net heterotrophic in

31 warm-water months (Jun–Nov). Although there is inter-annual variability in CO$_2$ flux in the

32 Rhode River, the annual mean condition is near carbon neutral. Measurement at high temporal

33 resolution across multiple years revealed that CO$_2$ flux and apparent trophic status can reverse

34 during a single 24 hr period. pCO$_2$ and CO$_2$ flux are mediated by temperature effects on

35 biological activity and are inverse to temperature-dependent physical solubility of CO$_2$ in water.

36 Biological/biogeochemical carbon fixation and mineralization are rapid and extensive, so

37 sufficient sampling frequency is crucial to capture unbiased extremes and central tendencies of

38 these estuarine ecosystems.

39

40 **1. Introduction**

41 Understanding the air–sea exchange of gases and establishing methodologies for accurate

42 measurements has been a decades-long focus of atmospheric scientists, oceanographers, and

43 biogeochemists seeking to understand interactions between oceans and the atmosphere and how

44 these interactions contribute to the global carbon cycle (Broecker et al., 1979; Wanninkhof,

45 1992, 2013). Coastal oceans and estuaries are ecosystems of interest for understanding the

46 complex nature and contribution of the land–sea interface to lateral mass transport of carbon

47 (Abril & Borges, 2005; Cai & Wang, 1998; Frankignoulle et al., 1998; Song et al., 2023) but also

48 with respect to the role these ecosystems play as both atmospheric CO$_2$ sources and sinks (Abril

49 & Borges, 2005; Chen et al., 2020; Dai et al., 2022; Jiang et al., 2008). The exchange of carbon

50 dioxide, methane, and other greenhouse gases (GHGs)between Earth's atmosphere and inland

51 waters, estuaries, coastal oceans are well-documented but not fully quantified (Abril & Borges,

52 2005; Cai, 2011; Laruelle et al., 2017; Raymond & Cole, 2001; Raymond et al., 2013; Van Dam

53 et al., 2019). CO_2 evasion from estuaries alone has been estimated at 15–17% of the total CO_2

54 input from oceans to the atmosphere (Chen et al., 2020; Laruelle et al., 2017), indicating the

55 regional and global significance of estuaries (Bauer et al., 2013; Frankignoulle et al., 1998; Jiang

56 et al., 2008). Yet, there is still great uncertainty surrounding the true net contributions of coastal

57 oceans, estuaries, and inland water bodies to the atmospheric loading of GHGs (Borges, 2005;

58 Chen et al., 2020; Herrmann et al., 2020; Joesoef et al., 2015; Laruelle et al., 2017; Raymond et

59 al., 2013; Van Dam et al., 2019).

60

61 To better understand the effects of estuaries on atmospheric GHG exchange and accumulation, it

62 is imperative that we understand their capacity and function as carbon sources and sinks and

63 ultimately how estuaries factor into the planet's overall global carbon budget (Herrmann et al.,

64 2020; Laruelle et al., 2017; Van Dam et al., 2019). Many attempts to characterize CO_2 flux in

65 estuaries and nearshore oceans (Chen et al., 2013; Herrmann et al., 2020; Rosentreter et al. 2021)

66 have relied on direct measurements using floating domes, tracer gases or, more recently, eddy

67 covariance methods (Laruelle et al, 2017; Van Dam et al., 2019). Because flux measurements are

68 time intensive, they tend to be temporally and spatially limited (Herrmann et al., 2020; Klaus &

69 Vachon, 2020). Using direct flux measurements to derive accurate gas transfer velocity

70 constants (K_o, the velocity of gas crossing the air-water boundary) enables models to be

71 parameterized to estimate K_o and compute gas flux. Thus, correlative models that incorporate

72 simultaneous environmental measurements such as wind and/or water velocity, factors that affect

73 turbulence at the air-water interface and promote gas exchange, have aided in the widespread

74 accumulation of gas flux estimates (Raymond & Cole, 2001; Van Dam et al., 2019; Wanninkhof,

75 2014). Gas transfer velocity constant models vary according to the habitat/system being observed

76 and chemical, physical, and biological factors present in each (e.g., lakes, rivers/streams,

77 estuaries, and oceans; Herrmann et al., 2020; Ho et al., 2016; Raymond & Cole, 2001; Van Dam

78 et al., 2019; Wanninkhof, 1992). To reduce uncertainty of computed gas fluxes, it is critical that

79 the appropriate K_o models are matched to a targeted ecosystem.

80

81 Coastal oceans and estuaries are exceptionally complex, frequently characterized by their relative

82 shallowness and how their freshwater inputs (riverine, surface, and groundwater) mix with salt

83   water (Chen et al., 2020). High nutrient and pollutant loading, due to urbanization and

84   eutrophication by humans, also have important effects on estuaries and coastal oceans (Freeman

85   et al., 2019). High spatial and temporal variability are hallmarks of estuaries.

86

87   Here we present a 3 year data set that combines high frequency (1 min interval) measurements of

88   dissolved and atmospheric CO_2 with co-located and continuous measurements of salinity, water

89   temperature, tidal cycling, and wind velocity, recorded at the Smithsonian Environmental

90   Research Center (SERC) dock, in the Rhode River, Maryland. To estimate hourly, daily,

91   seasonal, and annual CO_2 flux rates, we applied a CO_2 gas velocity constant model developed by

92   Van Dam et al. (2019) for the New River, North Carolina. This model is expressly designed for

93   application to shallow, well-mixed, microtidal estuaries located in the Mid-Atlantic coast of the

94   United States.

95

96   **2. Methods**

97   2.1 Study Location

98   The Rhode River is a tributary and subestuary of the Chesapeake Bay, a drowned river valley,

99   coastal plain estuary (Fig. 1). The Rhode River has been studied extensively by SERC staff and

100   colleagues for over 4 decades: nutrient chemistry (Jordan & Correll, 1991; Jordan et al., 1991),

101   phytoplankton ecology (Gallegos et al., 2010), color dissolved organic matter distribution

102   (Tzortziou et al., 2008; Tzortziou et al., 2011), and more recently, modeling of dissolved organic

103   carbon (DOC) input from freshwater and tidal marsh sources (Clark et al., 2020). Located on the

104   Bay's northwestern shore (38º52'N, 76º32'W), the Rhode River is bounded at its head by Muddy

105   Creek and at its mouth by the mainstem of the Chesapeake Bay. The Rhode River is a shallow

106   (mean depth = 2 m, max depth = 4.1 m), mesohaline (0 to 18 ppt), well-mixed, eutrophic

107   tributary with a length of approximately 5 km; its surface area is approximately 5 km^2 with a

108   shoreline perimeter of 39 km (Breitburg et al., 2008; Clark et al., 2018). A 0.21 km^2 tidal marsh

109   (Kirkpatrick Marsh) fringes the estuary at the mouth of Muddy Creek (Fig. 1). Tides are semi-

110   diurnal with a mean amplitude of approximately 30 cm, but water height can be strongly affected

111   by wind and weather events. Muddy Creek is the main freshwater source of the Rhode River and

112   has a maximum flow rate of 10.42 $m^3 \cdot s^{-1}$ and mean flow rate 0.18 $m^3 \cdot s^{-1}$ (mean flow = 15,552

113    $m^3 \cdot d^{-1}$; Clark et al., 2020; Clark et al., 2018; Jordan et al., 1986). The mean daily volume of

114   freshwater inflow from Muddy Creek is approximately 0.5% of the mean daily tidal exchange

115   volume, based on the Rhode River's area and mean tidal amplitude. In the absence of

116   measurements of the pH or pCO$_2$ of the freshwater entering the Rhode River from Muddy Creek

117   or other lesser freshwater inputs to the estuary, we are unable to report these pCO$_2$ or pH values.

118   However, given the exceedingly small overall volume of freshwater input to the Rhode River

119   from its surrounding watershed, it is not considered a river-dominated estuary so is not expected

120   to be substantially influenced by the chemical characteristics of this input. This is not to say there

121   is no freshwater influence, only that such influences are likely quite local when mixing with far

122   larger volumes of water from the Chesapeake Bay and therefore beyond the resolution of this

123   study.

124

125   Although the Rhode River is a model ecosystem that has been studied intensively for several

126   decades across many dimensions (Clark et al. 2018; Correll et al., 1992; Gallegos et al., 1992;

127   Jordan et al. 1991; Rose et al. 2019), no work to date has expressly characterized the nature and

128   dynamics of CO$_2$ flux between the river and the atmosphere.
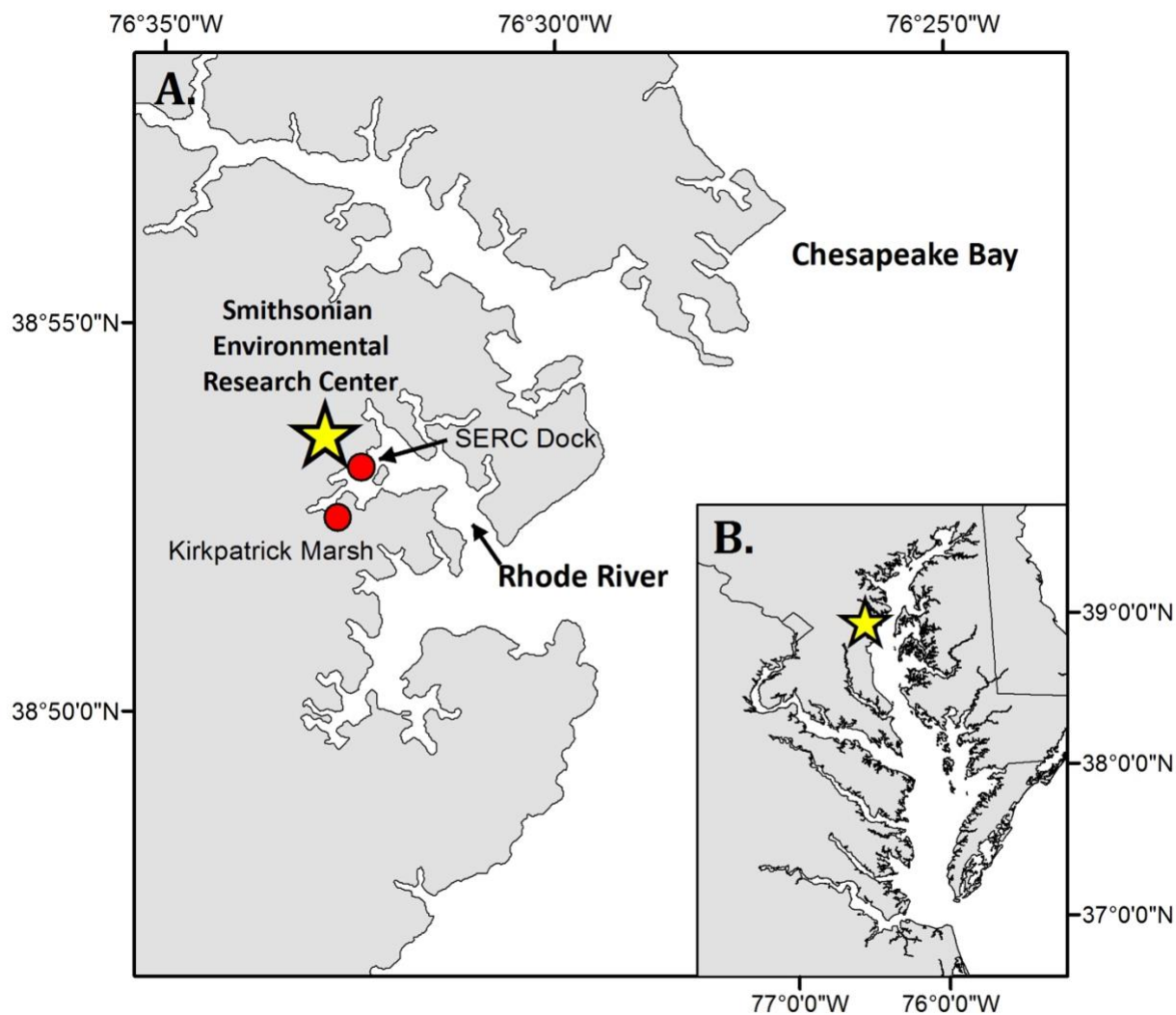
129
130 **Fig. 1.** Location of study site on the Rhode River, Edgewater MD (A), as situated in the
131 Chesapeake Bay (B). All pCO_2 and related water quality values reported were measured from the
132 SERC dock, that extends approximately 75 m from shore on Rhode River. Red circles indicate
133 location of dock and a tidal creek that drains the Kirkpatrick saltmarsh (marsh area = 0.21 km^2, 1
134 km up estuary from the dock).

135

136 <u>2.2 *In Situ* Measurements, Calculated Parameters and Quantities</u>

137 Continuous, automated environmental measurements were made in and above the Rhode River

138 during a 3 year period between 01 July 2018 and 01 July 2021. The purpose of these

139   measurements was to document fluctuations in aqueous pCO_2 on a fine time scale, from which

140   CO_2 flux between the water and atmosphere could be calculated.

141   <u>2.2.1 Aqueous CO_2 (pCO_{2water})</u>

142   To measure the CO_2 gradient ($\Delta C = pCO_{2water} - pCO_{2air}$) across the Rhode River surface waters

143   and its overlying atmosphere, measurements of pCO_2 were made with a non-dispersive infrared

144   (NDIR) detector. In the case of dissolved gas measurements, water was equilibrated continuously

145   with a spherical falling film equilibrator (Miller et al. 2019). Water from 1 m below the water's

146   surface was pumped and dispersed continuously over a 25.4 cm diameter sphere. The falling film

147   created on the sphere generates a gas exchange surface which forces CO_2 in the equilibrator

148   headspace into equilibrium with the water's CO_2 content (i.e. mole fraction = xCO_2 (μmol/mol).

149   Water exits the equilibrator via an airtight drain that prevents headspace contamination from

150   surrounding atmospheric air. Headspace gas circulates continuously in a closed loop through the

151   equilibrator, water trap and gas dehumidifier, past the NDIR, and back into the equilibrator.

152   Experimental observations concluded that spherical falling film equilibrators achieve 99%

153   equilibration of CO_2 within 10–15 mins, depending on whether step changes are from low to

154   high or high to low; details of the operation and performance of the falling film equilibrator are

155   described in Miller et al. (2019). Measurements were made at 1 min intervals at a pressure equal

156   to the ambient barometric pressure.

157

158   Measured raw CO_2 mole fractions (μmol/mol) were converted to partial pressures (μatm) using

159   equation 1. Minute-over-minute values were rounded down to the nearest hour and averaged to

160   provide hourly means. The mole fractions were then evaluated with corresponding water

161   temperature and salinity measurements following the methodology of Zeebe and Wolf-Gladrow

162   (2001) where saturation vapor pressure of water is calculated according to Weiss and Price

163   (1980) to determine pCO_{2water}.

164

165   $$pCO_{2water} = xCO_2 \cdot (p - pH_2O) \tag{1}$$

166

167   where

168   pCO_2 = partial pressure of CO_2 of water (μatm)

169   xCO_2 = mole fraction of CO_2 in water (μmol/mol)

170   p = total pressure = 1 atm

171 pH_2O = saturation vapor pressure of water (μatm)

172

173   2.2.2 Atmospheric CO_2

174   Every six hours, the sample gas stream was automatically diverted with programmed solenoid

175   control valves from the equilibrator to an atmospheric port located approximately 5 m above the

176   pier deck. During atmospheric sampling, 15 1-min interval measurements were made. To

177   account for inaccuracies during the transition period from equilibrator to atmospheric sampling,

178   the final eight measurements were averaged and the first seven were discarded. Similarly, the

179   first 30 measurements following switchover from atmospheric port to equilibrator were

180   discarded, to ensure measurements were fully equilibrated with water. For these atmospheric

181   measurements, the contribution of the vapor pressure of water to the total atmospheric pressure

182   of the open-air environment was considered negligible (i.e. $pH_2O = 0$ and $p = 1$), such that

183     $pCO_{2atm} = xCO_{2atm}$. As such, any potential differences are expected to fall well within the

184   measurement accuracy of the instrument (see below).

185

186   One advantage to using a shared NDIR sensor for aquatic and atmospheric samples is that any

187   minor effects of instrument drift will be reflected in both data streams, as opposed to two sensors

188   that drift independently of one another. Likewise, significant and sustained deviation from

189   typical local atmospheric variability will be captured during atmospheric sampling and can signal

190   the need for recalibration and assist with QA/QC of corresponding data from both streams. A

191   disadvantage of using a common sensor for both dissolved and atmospheric CO_2 measurements

192   is that it results in a mismatch in sampling frequency of the two. With this limitation in mind, we

193   chose a higher sampling frequency for aquatic measurements to better describe the inherently

194   higher variability in dissolved CO_2 in water vs. that in the atmosphere (Fig. 2).

195
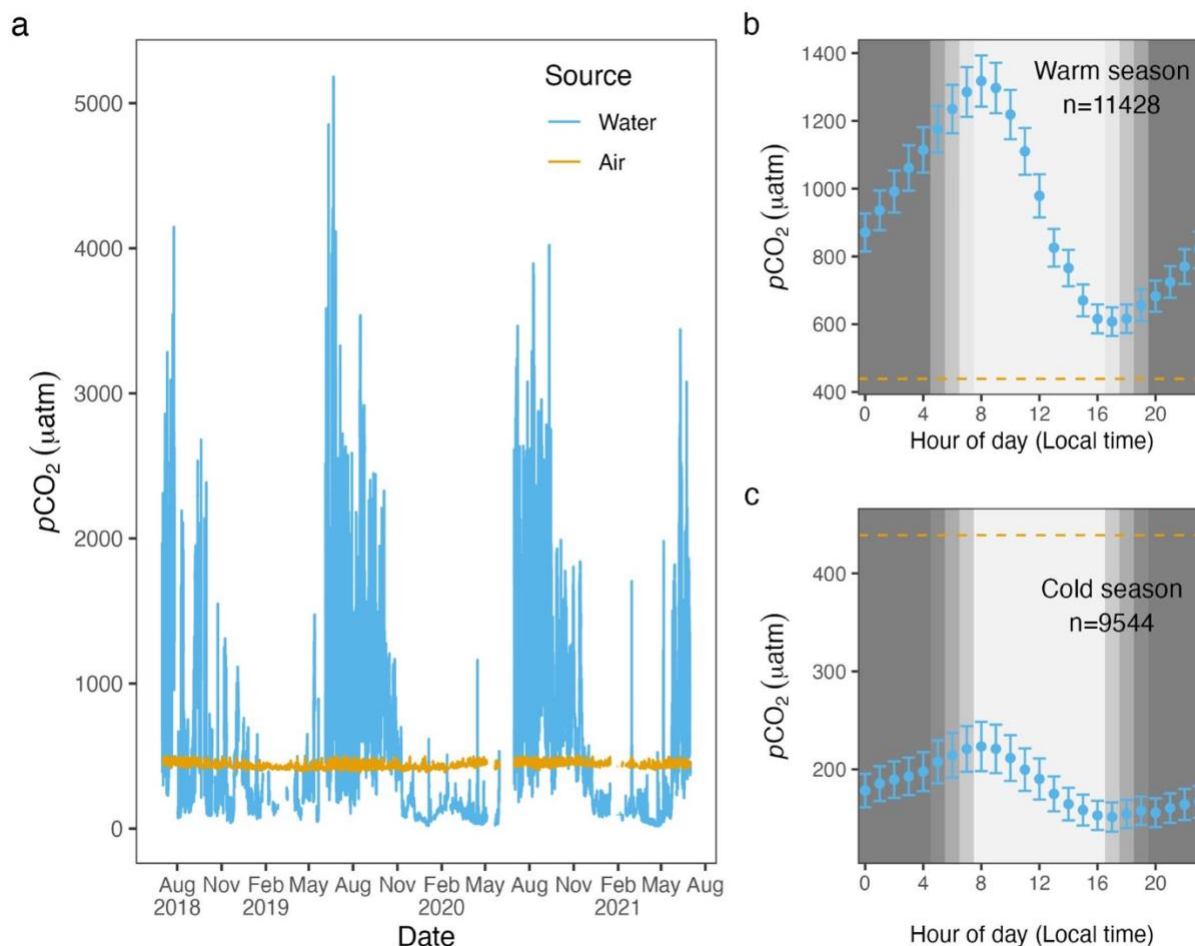
Fig. 2. Hourly pCO_{2water} (blue) and pCO_{2air} (goldenrod) values from 01 July 2018 to 01 July
2021 (panel a). The air-water CO_2 gradient, $\Delta C = pCO_{2water} - pCO_{2air}$ describes the directionality
of gas diffusion. Negative ΔC values (pCO_{2water} values falling below goldenrod demarcation)
represent gas movement from air to water and vice versa. Panels b and c depict mean pCO_{2water}
values (95% CI) for each hour of the day for warm and cold seasons, with the dashed lines equal
to the mean 3 yr value of pCO_{2air}.

202

Given the 3 yr time series and strong diel cycling of pCO_{2water} (and dissolved oxygen (DO), see

Figs. S1 and S2) in the Rhode River, we chose to aggregate aqueous minute-over-minute

measurements to mean hourly averages. Owing to the relative lack of short-term variability in

local atmospheric CO_2 concentrations (Fig. 2), we used linear interpolation to impute

atmospheric CO_2 concentrations during hours in between actual readings (6 hr gaps between

atmospheric measurements), which we assumed to be more realistic and reliable than Last

Observation Carried Forward (LOCF) methods, where the last observation is repeated for all

gaps until the next measurement is encountered, a method that has fallen out of favor, especially

211   for environmental time series data (Lachin, 2016). To determine if any inadvertent bias was

212   introduced by linear interpolation procedure, summary statistics of actual atmospheric readings

213   and actual readings + imputed CO_2 values were compared statistically. This approach enabled us

214   to take advantage of >25,000 time points throughout the 3 yr period of observation, providing

215   hourly resolution. Mean pCO_{2air} = 437 ± 20.0 μatm (Table 1), variability that falls well within

216   manufacturer's specifications (see section 2.2.4).

217

218   2.2.3 CO_2 gradient (ΔC)

219   ΔC was determined by subtraction, pCO_{2water} – pCO_{2air}, where positive ΔC values correspond to

220   higher CO_2 concentrations in the water, tending toward movement from water to air (outgassing

221   or evasion, where Rhode River = CO_2 source), and negative values that signal CO_2 transport

222   from air to water (dissolution, where Rhode River = CO_2 sink). Figure 2 shows pCO_{2water} and

223   pCO_{2air} plotted on an hourly basis for the 3 yr period beginning 01 July 2018 and ending 01 July

224   2021. Across this period, ΔC was predominantly negative during cold months and predominantly

225   positive during warm months when pCO_{2water} tended to reach the highest values of the year, but

226   ΔC sometimes reversed sign due to occasional extreme day-time photosynthetic drawdown of

227   CO_2 (Fig. 2).

228

229   2.2.4 Accuracy of CO_2 measurements

230   Estimated accuracy of the spherical falling film equilibrator and NDIR sensor (SenseAir K30,

231   https://senseair.com/) combination were experimentally determined in the lab and found to

232   measure water equilibrated with known gas concentrations to be within the ±1% uncertainty

233   limits of the of certified standard gas mixtures used, and well within the published accuracy

234   specification of the SenseAir K30 (i.e., ± 30 ppmv ± 3% of instrument reading). Experimental

235   analysis by Martin et al. (2017) report even higher accuracy when relative humidity and

236   atmospheric pressure are controlled for. Details on performance of the spherical falling film

237   equilibrator, such as accuracy, precision, and time constants can be found in Miller et al. (2019).

238   Although SenseAir offers automated calibration via long term comparisons to atmospheric

239   readings, this feature was deactivated. The K30 NDIR was periodically validated using standard

240   zero CO_2 (nitrogen) and standard certified span gases at intervals of one to two months during

241   the study period. Although the K30 was never observed to drift beyond its factory specifications,

242   the sensor was occasionally re-calibrated in the lab, and measured values were accepted without

243   adjustment.

244

245   CO_2 measurements were downloaded to a database at approximately two-week intervals during

246   the observation period. Data were graphed and reviewed visually, in combination with twice

247   weekly observations of equilibrator function recorded in an accompanying notebook. Anomalous

248   data were flagged and excluded from data analysis (e.g., flooding or clogging events that

249   interrupted proper equilibration.)

250

251   2.3 Co-located water quality and atmospheric measurements

252   This water quality station at the SERC dock is a long-term node of the Maryland Department of

253   Natural Resources "Eyes on the Bay" Chesapeake Bay tidal water monitoring program, and has

254   been operated by the SERC since 1986. Water quality and atmospheric data are maintained by

255   the MarineGEO Upper Chesapeake Bay Observatory and can be accessed online (Benson et al.,

256   2023). A YSI EXO2 sonde was positioned 1 m below the water's surface and in proximity (~2.5

257   m distance) to the submerged water pump that fed the $p\mathrm{CO}_2$ equilibrator. Sonde measurements

258   were made at 6 minute intervals and aggregated to 1 hr averages. The published accuracy

259   specifications for the YSI sonde are as follows: temperature: ±0.01 ºC (-5º to 35º C); salinity:

260   ±1% of reading or 0.1 ppt (0–70 ppt); dissolved oxygen: ±0.1 mg/L or 1% of reading (0 to 20

261   mg/L). Discrete measurements of temperature and salinity were made with a handheld YSI

262   Professional Plus 2030 with Quattro Cable instrument, with the following specifications:

263   temperature: ±0.02 ºC (-5º to 70º C); salinity: ±1% of reading or 0.1 ppt (0–70 ppt); dissolved

264   oxygen: ±0.2 mg/L or 2% of reading (0 to 20 mg/L). Equilibrator temperature was measured

265   with a probe (EDS model OW-TEMP-B3-12xA) accurate to ±0.5 ºC (-10º to 85 ºC). Discrete

266   measurements were routinely compared with the sonde to corroborate measurement agreement.

267   Wind speed measurements were made using a sonic anemometer (Vaisala WXT-520 weather

268   transmitter) mounted 7 m above the mean low tide height of the water and located directly above

269   the $p\mathrm{CO}_2$ equilibrator.

270

271   2.4 Data Processing

272   Data included in this study span 01 Jul 2018 to 01 Jul 2021.

273   2.4.1 Gas-specific solubility

274   To determine the purely physical effects of temperature and salinity on CO_2 solubility, gas-

275   specific solubility values K_0 (mmol · m^{-3} · µatm^{-1}) were calculated across the 3 yr observation

276   period using water temperature and salinity measurements in combination with pCO_{2water} values,

277   according to Weiss and Price (1980) at 1 hour intervals.

278

279   2.4.2 Gas transfer velocity estimation (k)

280   Given the similarities between the Rhode River and New River estuaries (e.g., shallow,

281   microtidal estuaries with slow water velocity and strong diel cycles in pCO_2 and DO), we chose

282   to parameterize gas transfer velocity k (cm · h^{-1}) standardized to the unitless Schmidt number

283   600 (k_{600}) according to the estuary-specific k parameterization model developed by Van Dam et

284   al. (2019). Van Dam et al. (2019) determined that k correlated with wind speed differently during

285   daytime versus nighttime hours (linear vs. parabolic relationships). Wind speed data were

286   collected during the 3 yr period from a sonic anemometer located on the SERC dock directly

287   above the equilibration system and approximately 7 m above the water's surface at mean low

288   tide height. For the analysis, windspeeds were standardized for a height of 10 m following a

289   power-law relationship, $U_{10} = U_7 * (10/7)^{0.15}$ (Saucier, 2003). Following Van Dam et al.,

290   wind speed data were binned to 1.5 m s^{-1} intervals for day and night readings and raw values

291   replaced by the mean wind speed for each bin. The median binned windspeed over the Rhode

292   River was 2.2 m s^{-1}, regardless of time of day or season. Recorded windspeeds never exceeded

293   10m s^{-1} and were dominated by much lower values (Fig. S1). Unlike the New River Estuary, the

294   Rhode River's windspeed profile does not differ much between day and night, nor across season.

295   For this reason, we chose to use the most conservative k_{600} formulation from Van Dam et al

296   (2019), that combines day and night winds to estimate k_{600}.

297

298   Wind speed was used to parameterize k_{600} as follows:

299

300                  $$k_{600} = 1.5 * U_{10} + 4.2 \hspace{3cm} (2)$$

301

302   where U_{10} = mean of binned wind speed at 10 m above the water's surface (m · s^{-1}).

303

304   2.4.3 CO_2 flux

305   Using continuous, parallel 3 yr records (01 July 2018 to 01 July 2021) of dissolved and

306   atmospheric pCO_2, water temperature, salinity, and wind speed (at standard 10m height, U_{10}),

307   CO_2 flux was derived according to the equation:

308

309        $$CO_2 \text{ flux} = k_{600} \cdot K_0 \cdot \Delta C \cdot (600 / Sc)^{-0.5} \tag{3}$$

310   where

311   CO_2 flux = the rate and direction of CO_2 mass moving between water and gas phases

312        $(mmol \cdot m^{-2} \cdot hr^{-1})$

313   k_{600} = gas transfer velocity $(cm \cdot hr^{-1})$, normalized to a common Schmidt number

314        $(Sc = 600)$

315   K_0 = gas-specific solubility for CO_2 $(mmol \cdot m^{-3} \cdot \mu atm^{-1})$

316   ΔC = air-water concentration gradient (μatm)

317   Sc = Schmidt number

318

319   Note: CO_2 flux calculations require conversion from traditional k_{600} units $(cm \cdot hr^{-1})$ to $(m \cdot hr^{-1})$

320   from ΔC units (μatm) to (atm) prior to calculation.

321

322   2.4.4 Day/Night Designation

323   To differentiate daytime from nighttime hours, we used the position of the measurements

324   (latitude) in the Rhode River, combined with the local date and time. This approach enabled us to

325   uniformly designate various environmental measurements as happening during the day or night

326   (R package "LakeMetabolizer", Winslow et al., 2016).

327

328   2.4.5 Seasonality

329   We chose to break the year into two 6 month periods based seasonal water temperature shifts,

330   designating June–November as "warm-water months" when water temperatures averaged $23.2 \pm$

331   6.90 °C. (mean $\pm$ 1 sd) and December–May as "cold-water months", 10.9 ± 5.66 °C (Figs. S1and

332   S2).

333

334

335   2.4.6 Effect size

336   Owing to the large number of observations available for comparison in this study, the likelihood

337   of finding statistically significant results is quite high. Whether such statistical results by

338   themselves connote practical and informative differences can be difficult to discern. Effect sizes

339   (Omega-squared, ω^2) were calculated according to two-factor ANOVAs where independent

340   variables were investigated by season (cold-water vs. warm-water season), day/night period and

341   the interaction of season and day/night. The independent variables compared were: K_0, CO_2 flux,

342   ΔpCO_2, k_{600}, pCO_{2air}, pCO_{2water}, and wind speed. To account for temporal autocorrelation and

343   lack of independence of observations that are typical of environmental time series data, we

344   corrected for overinflation in the residual mean square used in the effect size calculations by

345   removing the autocorrelation present within residuals, leaving the white-noise component as the

346   unbiased estimate of residual variability (Cochrane-Orcutt procedure, R package "orcutt", Spada

347   et al., 2018).

348

349   **3. Results and Discussion**

350   3.1 Daily and Seasonal Cycling of pCO_2

351   Hourly averaged measurements of pCO_{2water} in the Rhode River across three years revealed

352   strong diel and seasonal cycling (Fig. 2). Mean and maximum pCO_{2water} were significantly higher

353   in warm-water vs. cold-water months (Table 1). During warm-water months (Jun–Nov) daily

354   oscillations of pCO_2 frequently transit from far above to below ambient atmospheric conditions

355   over the course of the day, only to reverse direction (from low to high) during the nighttime

356   hours (Fig. 2). During the summer, pCO_{2water} levels sometimes shifted by as much as 4500 μatm

357   in both directions during a single 24 hr period (Fig. 2). This pattern is consistent with

358   biologically driven cycling whereby very high early morning pCO_{2water} conditions are depleted

359   by net photosynthetic activity (inorganic carbon fixation) over the course of the day, but high

360   pCO_{2water} is restored by respiration in the benthos and water column at night (Song et al. 2023).

361   Comparing dissolved oxygen (DO) over the same period, similar harmonic cycling is observed,

362   but maximums and minimums of pCO_2 and DO were inversely related (Fig. S1), hallmarks of a

363   production/respiration driven system (Herrmann et al., 2020; Van Dam et al., 2019).

364

365 **Table 1.** Descriptive statistics comparing seasonality of $p\text{CO}_2$, CO_2 flux and associated
366 parameters in cold-water (Dec–May) and warm-water seasons (Jun–Nov).
367

Season	Time Period	Variable	Units	N	Mean	Min	Max	SD
overall	-	**CO_2 flux**	**mmol · m^{-2} · hr^{-1}**	**20971**	**-0.09**	**-4.89**	**11.18**	**1.823**
cold	day	CO_2 flux	mmol · m^{-2} · hr^{-1}	4494	-1.39	-4.89	8.26	1.134
cold	night	CO_2 flux	mmol · m^{-2} · hr^{-1}	5050	-1.39	-4.66	5.24	0.927
warm	day	CO_2 flux	mmol · m^{-2} · hr^{-1}	6007	1.18	-3.95	11.18	1.731
warm	night	CO_2 flux	mmol · m^{-2} · hr^{-1}	5421	0.78	-3.97	8.05	1.467
overall	-	**K_0**	**mmol · m^{-3} · μatm^{-1}**	**20971**	**0.04**	**0.03**	**0.07**	**0.011**
cold	day	K_0	mmol · m^{-3} · μatm^{-1}	4494	0.05	0.03	0.07	0.009
cold	night	K_0	mmol · m^{-3} · μatm^{-1}	5050	0.05	0.03	0.07	0.008
warm	day	K_0	mmol · m^{-3} · μatm^{-1}	6007	0.03	0.03	0.06	0.007
warm	night	K_0	mmol · m^{-3} · μatm^{-1}	5421	0.04	0.03	0.07	0.008
overall	-	**k_{600}**	**cm · hr^{-1}**	**20971**	**7.86**	**5.57**	**18.36**	**2.047**
cold	day	k_{600}	cm · hr^{-1}	4494	8.71	5.57	16.33	2.251
cold	night	k_{600}	cm · hr^{-1}	5050	7.74	5.57	18.36	2.081
warm	day	k_{600}	cm · hr^{-1}	6007	7.92	5.57	18.36	1.868
warm	night	k_{600}	cm · hr^{-1}	5421	7.20	5.57	18.36	1.751
overall	-	**ΔC**	**μatm**	**20971**	**154**	**-436**	**4750**	**645.8**
cold	day	ΔC	μatm	4494	-239	-436	1553	220.9
cold	night	ΔC	μatm	5050	-256	-434	1204	164.2
warm	day	ΔC	μatm	6007	570	-399	4750	745.5
overall	-	**$p\text{CO}_{2air}$**	**μatm**	**20971**	**437**	**387**	**500**	**20.0**
cold	day	$p\text{CO}_{2air}$	μatm	4494	430	390	497	16.0
cold	night	$p\text{CO}_{2air}$	μatm	5050	432	387	499	17.8
warm	day	$p\text{CO}_{2air}$	μatm	6007	439	390	499	20.7
warm	night	$p\text{CO}_{2air}$	μatm	5421	443	387	500	21.5
overall	-	**$p\text{CO}_{2water}$**	**μatm**	**20971**	**591**	**15**	**5182**	**651.8**
cold	day	$p\text{CO}_{2water}$	μatm	4494	191	15	1982	220.9
cold	night	$p\text{CO}_{2water}$	μatm	5050	176	17	1638	163.9
warm	day	$p\text{CO}_{2water}$	μatm	6007	1009	47	5182	752.6
warm	night	$p\text{CO}_{2water}$	μatm	5421	844	38	4855	632.2
overall	-	**wind speed**	**m · s^{-1}**	**20971**	**2.4**	**0.1**	**9.8**	**1.42**
cold	day	wind speed	m · s^{-1}	4494	3.1	0.3	8.9	1.53
cold	night	wind speed	m · s^{-1}	5050	2.4	0.3	9.1	1.45
warm	day	wind speed	m · s^{-1}	6007	2.5	0.1	9.8	1.28
warm	night	wind speed	m · s^{-1}	5421	2.0	0.1	9.1	1.23

368
369 On the seasonal timescale, $p\text{CO}_2$ was consistently lowest and DO highest during cold-water
370 months of the year (Dec–May; Fig. S1). Importantly, for both gases the temporal variability (diel

371   cycling; Fig. S2) was most constrained during cold-water months across years, strongly

372   suggesting that carbon fixation exceeds respiration for prolonged periods (weeks to months). In

373   contrast, during warm-water months (Jun–Nov), photosynthesis/carbon fixation and respiration

374   are more evenly balanced, compensating one another over 24 hr periods (i.e., respiration >

375   productivity at night and productivity > respiration during daylight hours; Fig. 2).

376

377   <u>3.2 Air-water concentration gradient = ΔC (µatm)</u>

378   When hourly pCO_{2water} and pCO_{2air} values (composed of 4 hourly measurements and 20

379   interpolated values per day) were plotted across the three years of observation, the diel and

380   seasonal cycles of pCO_{2water} are evident. As expected, atmospheric concentrations of CO_2

381   remained relatively constant compared with aqueous loads. When the mean raw pCO_{2air}

382   measurements (mean = 435.1, 95% CI [434.4, 435.7]) were compared with raw pCO_{2air}

383   measurements + imputed estimates (mean = 435.4, 95% CI [435.2, 435.7]) no statistical

384   difference was observed, indicating that no substantial bias was introduced by linear

385   interpolation of atmospheric measurements.

386

387   Although nearshore atmospheric CO_2 concentrations are expected to vary more than those in

388   isolated well-mixed atmosphere (e.g., at the Mona Loa Observatory), annual mean values were

389   consistent and within the published uncertainty of the K30 NDIR sensor, when compared with

390   global measurements conducted at Mona Loa (Thoning et al., 2023). Local perturbations (e.g.,

391   effects of terrestrial photosynthetic drawdown when wind is absent) were apparent in

392   measurements (Fig. 2) but there were no instances when the measured local atmospheric values

393   were suspiciously high or low for days on end, as compared with expected global mean

394   atmospheric values for the time period (i.e., 408–416 ppmv; https://www.co2.earth/annual-co2,

395   Thoning et al., 2023). This lack of sustained anomalous deviation served as additional

396   confirmation that the K30 was functioning properly and had not drifted outside its calibration

397   range. Importantly, given the extreme diel cycling and seasonal variability of the Rhode River's

398   pCO_{2water}, the absolute accuracy necessary for determining year-over-year changes in

399   atmospheric or ocean pCO_2 is not a requirement for these CO_2 flux calculations which rely on

400   relative differences between water and atmospheric measurements.

401

402   Hourly air-water concentration gradient values = ΔC (μatm) were calculated and plotted across

403   the three years of study (Fig. 2). During warm months, pCO_{2water} routinely shifts from

404   supersaturated to sub-atmospheric and back again, over the course of 24 hours (e.g., between

405   >2000 μatm and <410 μatm on a single day). These large daily swings in pCO_{2water} produced

406   concomitant directional reversals of ΔC ($pCO2_{water} - pCO_{2air}$), which result in longer term

407   averaged gradients (e.g., multi-day, multi-week averages) near zero (Fig. 2). In contrast, most of

408   the time during cold-water months is spent in a state of sub-atmospheric pCO_{2water} (under-

409   saturation with respect to overlying atmosphere), resulting in ΔC values that are negative and

410   which promote movement of CO_2 from the atmosphere into the water.

411

412   3.3 Gas-specific solubility (K_0)

413   To account for the physical effects of temperature and salinity on the solubility of CO_2 in

414   estuarine water, K_0 was calculated by methods of Weiss and Price (1980). K_0 varied strongly

415   across seasons over the 3 yr observation period. The maximum annual range = 0.027 to 0.071

416   mmol $\cdot$ m^{-3} $\cdot$ μatm^{-1}; mean cold-water months = 0.051 and mean warm-water months = 0.035

417   mmol $\cdot$ m^{-3} $\cdot$ μatm^{-1}, confirming that CO_2 was most soluble during winter and least soluble in

418   summer (Fig. 3). This is inverse to observed dissolved CO_2 values: pCO_{2water} was lowest and

419   least variable during winter and highest and most variable during summer (Fig. 2, Table 1)

420   suggesting that solubility, in and of itself, plays only a minor and non-limiting role in pCO_{2water}

421   in the Rhode River. Effect size (ω^2) estimates indicated that the greatest proportion of variability

422   in K_0 was associated with season, vs. day/night or the interaction of the two (Table 2).

423
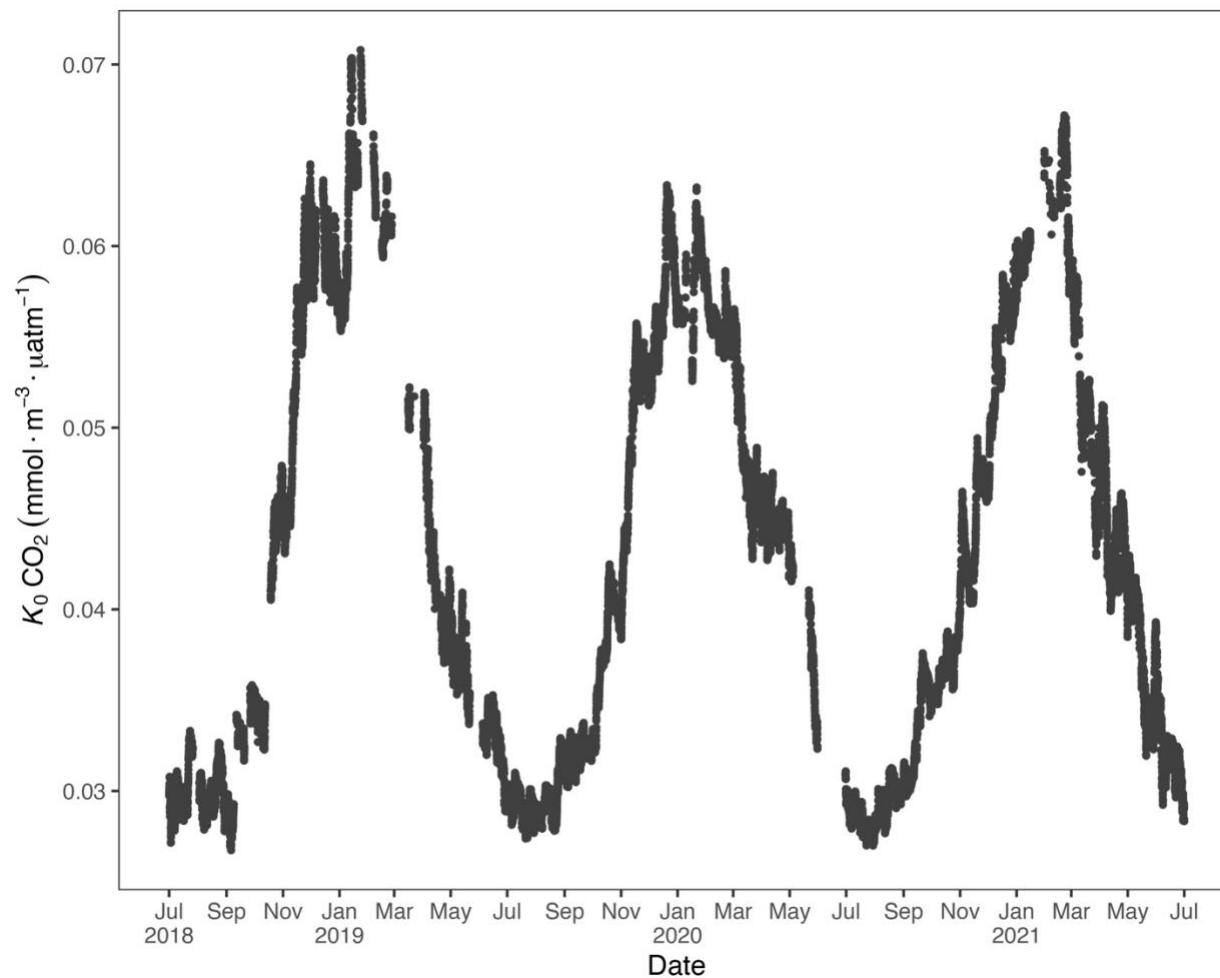
Fig. 3. Gas-specific solubility (K_0) for CO_2 based on water temperature and salinity.
Units are mmol m^{-3} µatm^{-1} in the Rhode River (01 Jul 2018 to 01 Jul 2021).

426 **Table 2.** Contrast effect sizes based on two-factor ANOVA where independent variables were
427 compared by season (cold-water season = Dec–May vs warm-water season = Jun–Nov),
428 day/night period and the interaction of the two. ω^2 is a measure of effect size, estimating the
429 proportion of total variance explained by each parameter. Effect sizes were corrected for inherent
430 temporal autocorrelation using the Cochrane-Orcutt procedure (Spada et al., 2018).
431

Variable	Factor	Effect Size (ω^2)
K_0	Season	0.0300
K_0	Day/Night	0.000575
K_0	Season:Day/Night	0.0000140
CO_2 flux	Season	0.415
CO_2 flux	Day/Night	0.00295
CO_2 flux	Season:Day/Night	0.00301
ΔC	Season	0.310
ΔC	Day/Night	0.00501
ΔC	Season:Day/Night	0.00333
k_{600}	Season	0.00164
k_{600}	Day/Night	0.00269
k_{600}	Season:Day/Night	0.0000549
pCO_{2air}	Season	0.000137
pCO_{2air}	Day/Night	0.0000134
pCO_{2air}	Season:Day/Night	0.00000137
$pCO_{2\ water}$	Season	0.188
$pCO_{2\ water}$	Day/Night	0.00275
$pCO_{2\ water}$	Season:Day/Night	0.00191
wind speed	Season	0.00711
wind speed	Day/Night	0.0186
wind speed	Season:Day/Night	0.000182

432

433 ### 3.4 Temperature/Biology ratio

434 To independently parse the magnitude of the physical versus biological forcing of pCO_{2water}, we

435 estimated the Takahashi's Temperature/Biology ratio (Takahashi et al., 2002) to compare the

436 influence of temperature and biological activities on pCO_{2water}. Across the 3 year period, we

437 found that just $26.0 \pm 4.0\%$ (mean $\pm$ SD) of forcing was attributable to the effect of temperature

438 on solubility, confirming that the predominant driver of pCO_{2water} in the Rhode River is indeed

439 biological activity (75%, Table 3). These patterns demonstrate the outsized role that biological

440 processes play in shaping pCO_{2water} in nearshore marine and estuarine ecosystems (Dai et al.,

441 2022; Van Dam et al., 2019).

442

443
444 **Table 3**. Takahashi Temperature/Biology Ratio (Eq. 5a From Takahashi et al. 2002).
445

Year	N	$\Delta p CO_2\_bio$	$\Delta p CO_2\_temp$	T/B ratio
2018	4416	3193.0	765.8	0.240
2019	8760	3669.8	1019.6	0.278
2020	8784	2772.1	846.0	0.305
2021	4345	2356.1	507.2	0.215
Overall	26305	3701.5	926.4	0.250

446

447

448   3.5 Gas transfer velocity (k_{600})

449   Gas transfer velocity is affected by both mass transfer from molecular diffusion driven by ΔC

450   (i.e. CO_2 gradient between water and atmosphere) and momentum transfer linked to external

451   environmental forces that enhance turbulence at the air-water boundary layer (Ho et al., 2016;

452   Raymond & Cole, 2001; Van Dam et al., 2019). Van Dam et al. (2019) validated the use of wind

453   speed at 10 m above the water's surface (U_{10}) to estimate gas transfer velocities of CO_2 that were

454   standardized to a Schmidt number of 600 (k_{600}) by comparing estimated values to k_{600} values

455   derived directly from eddy covariance CO_2 flux measurements. Given the relative uniformity of

456   wind speed over the Rhode River where median binned U_{10} windspeed (converted from U_7

457   measurements) was 2.2 m · s^{-1} regardless of time of day or season, and that maximum values

458   rarely exceeded 10 m s^{-1} (Table 1, Fig. S1), we chose to use the most conservative estuarine-

459   specific parameterization of k_{600} (Van Dam et al., 2019) (Eq. 2). The mean overall Rhode River

460   k_{600} value for CO_2 (mean ± SD, 7.86 ± 2.05 cm · hr^{-1}) was of comparable magnitude to that of

461   the New River Estuary, NC (9.37 ± 9.47 cm · hr^{-1}. However, wind speed varied far less on the

462   Rhode River than the New River estuary and day/night explained more variability in wind speed

463   than season. Because wind speed directly influenced the formulation of k_{600} (Eq. 2), the effect

464   size of day/night is similarly greater than the seasonal effect on gas transfer velocity (Table 2).

465   Nevertheless, effect sizes (ω^2) indicate that "season" explained at least 10 times more of the

466   observed variance of $p CO_2 water$, $p CO_2 air$, air-water concentration gradient, CO_2 flux, and gas-

467   specific solubility than "day/night" or their interaction (Table 2). Given the minor freshwater

468   input and microtidal nature of the Rhode River, we do not believe that lateral water velocity and

469   bottom turbulence appreciably affect the gas transfer velocity of CO_2 here, although we did not

470   investigate possible influences explicitly.

471

472   Importantly, in coastal marine and estuarine habitats, ΔC can shift as much as several thousand

473   µatm per day due to diel cycling associated with CO_2 production and depletion (Figs. 2, S2). The

474   uncertainty surrounding gas transfer velocity parameterization can represent a major source of

475   error in CO_2 flux calculations (Frankignoulle et al., 1998; Upstill-Goddard, 2006; Wanninkhof &

476   McGillis, 1999); however, small errors in k_{600} have far less effect on CO_2 flux calculations in

477   estuaries which experience pCO_2 swings of several thousand µatm during a single day, compared

478   with more stable conditions of the open ocean where interannual ranges of pCO_2 are typically far

479   less (Van Dam et al., 2019).

480

481   <u>3.6 CO_2 flux - Seasonality and Interannual Variation</u>

482   CO_2 flux was determined according to Eq. 3 using hourly ΔC measurements, CO_2 solubility

483   values (K_0) calculated according to temperature and salinity, and estuary-specific standardized

484   gas transfer velocities (k_{600}) of Van Dam et al. (2019). CO_2 flux was plotted across the three

485   years of observations at hourly and monthly intervals (Fig. 4a-b). As observed with pCO_2, CO_2

486   flux in the Rhode River was shown to be strongly seasonal. Given the similarity in windspeed

487   across seasons (Fig. S1), the effect of differential mean ΔC and variation between warm- and

488   cold-water seasons (Fig. 2, Table 1) almost certainly drives the observed seasonal differences in

489   CO_2 flux (Fig. 4). Again, the specific solubility of CO_2 is greatest at low temperatures, yet this is

490   contrary to the observed mean pCO_{2water} patterns, pointing toward a biological mechanism for

491   pCO_2, ΔC, and ultimately, CO_2 flux. The effect size of season on CO_2 flux was two orders of

492   magnitude greater than either day/night or the season day/night by interaction (Table 2).

493

494
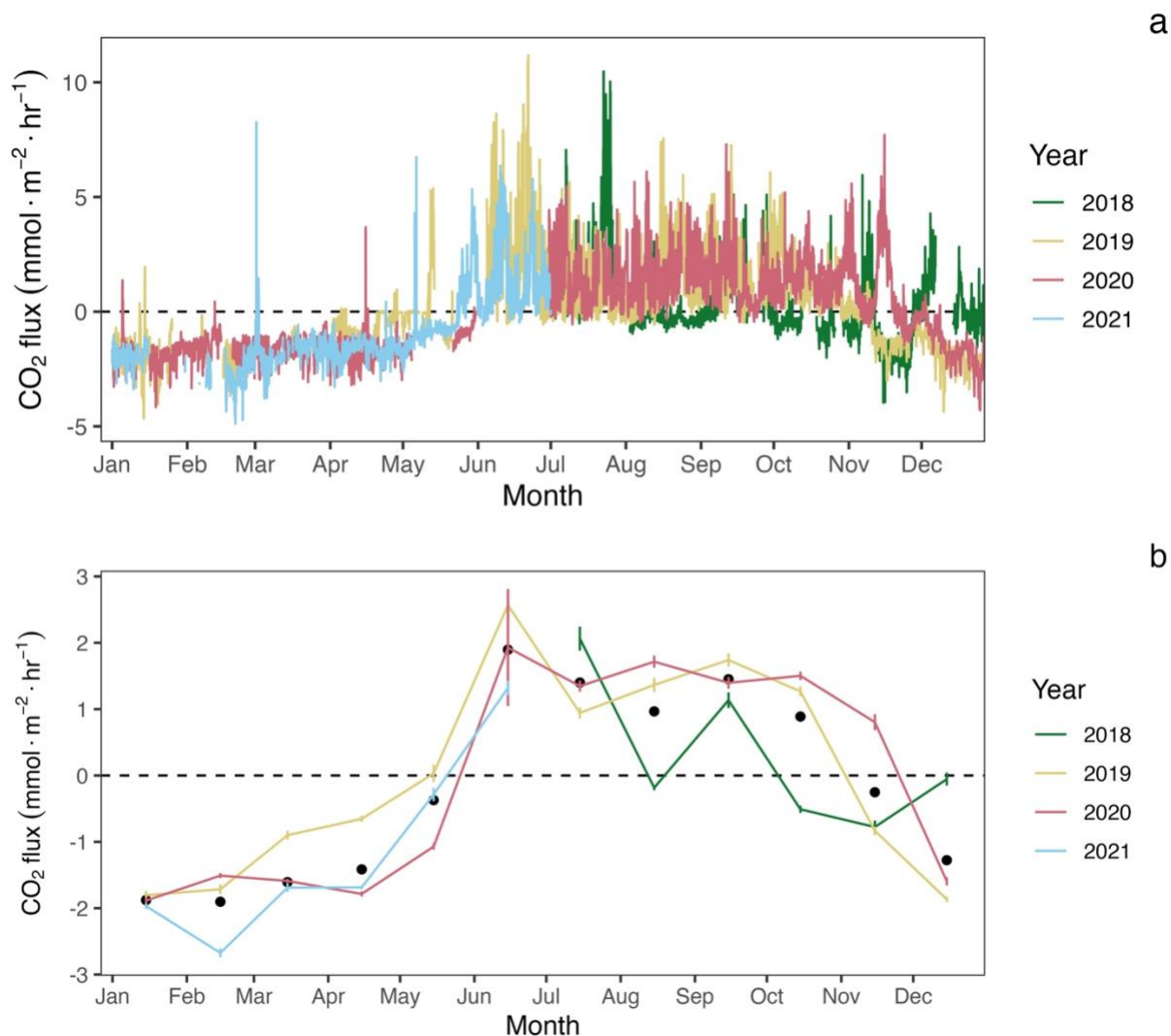
Fig. 4. CO_2 flux estimates by year: a. Hourly, b. Monthly average CO_2 flux estimates with 95% confidence limits. Black dots in panel b indicate mean monthly fluxes across years.

497

Among years, pCO_{2water} and CO_2 flux largely repeat themselves, with dissolved CO_2 becoming

consistently sub-atmospheric and CO_2 flux going negative (gas exchange from atmosphere to

water) between December and May and abruptly transitioning to much higher maximum, yet

variable pCO_{2water} values with net positive CO_2 fluxes from June through November (Figs. 2 and

4). Monthly averaged CO_2 fluxes are consistent among years (Fig. 4b), with net positive CO_2

fluxes (heterotrophic conditions) between June and November and negative (autotrophic) fluxes

dominating when water temperatures are cold, between December and May. Despite the overall

505   similarities in seasonal CO_2 flux, inter-annual patterns can vary considerably. When hourly CO_2

506   flux values were averaged for the year, the Rhode River in 2019 was shown to have a net

507   positive flux but a net negative flux in 2020. When scaled for the year, 2019 outgassed CO_2 from

508   the water to the atmosphere at a rate of 2215.08 mmol $\cdot$ m^{-2} $\cdot$ yr^{-1} (95% CI = 1816.88, 2613.29).

509   The annual net flux rate in 2020 was negative (i.e. CO_2 moved from the atmosphere into the

510   river) at a rate of -1361.31 mmol $\cdot$ m^{-2} $\cdot$ yr^{-1} (95% CI = -1723.60, -999.01).

511

512   At shorter time scales, such as comparing the same week of the year among years, we sometimes

513   observed vast differences in the magnitude and direction of CO_2 flux (Fig. S3), signaling

514   differences in seasonal conditions between years. Transient events can also result in deviations

515   from otherwise typical CO_2 flux conditions. For example, the period from July 2018 to Jan 2019

516   deviated from other years as CO_2 flux was more erratic, with intermittent periods of negative and

517   positive CO_2 flux extending later into the winter season than in other years. When water

518   temperatures are compared among years, 2018 was shown to be more inconsistent, with more

519   pronounced temperature shifts and reversals than in 2019 or 2020 (Fig. S1). Salinities remained

520   relatively low for the latter half of 2018 into early 2019, reflecting wetter conditions (Fig. S1).

521   There were also two rapid salinity declines (>4 ppt reductions) in July and October 2018, likely

522   associated with strong precipitation events. These events were both followed by immediate

523   spikes in chlorophyll-*a* concentration to levels exceeding 200 µg $\cdot$ L^{-1}, indicative of

524   phytoplankton bloom conditions. From 2018 to 2021, chlorophyll-*a* levels of this magnitude and

525   greater were generally confined to cold-water months (Dec–May; Fig. S1 Erratic water

526   temperature and salinity are also reflected in more variable gas-specific solubility (K_0) for CO_2 in

527   2018 than later years (Fig. 3).

528

529   Gallegos et al. (1992) documented predictable phytoplankton blooms associated with freshets in

530   the Rhode River, when nutrient-rich freshwater inundates the estuary, not from point and non-

531   point sources within the local Rhode River watershed, but instead from the enormous watershed

532   that feeds the Susquehanna River, the primary source of freshwater input into the Chesapeake

533   above the Potomac as well as >50% of the entire Bay's freshwater (U.S. Geological Survey,

534   2023). Unlike river dominated estuaries, in the Rhode River estuary, volumetric influxes from

535   the Chesapeake Bay end member far exceed freshwater input from the Muddy Creek and

536   secondary tributaries. In the Rhode River, phytoplankton blooms result in the temporary

537   depletion of pCO_{2water}, followed by a spike, as phytoplankton senesce and organic carbon is

538   decomposed/re-mineralized back into inorganic carbon. Episodic, short-lived occurrences like

539   these demonstrate how immediate small scale biological forcing, can be coupled with, and

540   catalyzed by, distant large-scale weather and hydrological events. These in turn can influence

541   pCO_2 flux variations within seasons and among years (Fig. 3 and S3; and Chen et al., 2020).

542

543   Overall, except for wind speed, the effect sizes for the other six measured or calculated variables

544   were shown to be greatest for season vs. day/night or the interaction of season x day/night, and in

545   all cases the season effect was greater by at least 1 order of magnitude (Table 2). Seasonality has

546   10 to 1000 times more explanatory power than other variables investigated as estimated by ω^2

547   (Table 2).

548

549   3.7 Diel Cycling

550   The notion that estuaries are predominantly heterotrophic systems that invariably outgas more

551   CO_2 to the atmosphere than they absorb has been a long-held view (Abril et al., 2000; Borges et

552   al., 2004; Cai, 2011; Cai et al., 2000; Chen, 2013; Frankignoulle et al., 1998, Gattuso et al.,

553   1998). However, more recently investigators have realized that physical and hydrological

554   characteristics, geographical location, size, and biological and biogeochemical activities may

555   individually, or together, influence CO_2 flux in estuaries and therefore contributions to

556   atmospheric chemistry (Brodeur et al. 2019; Caffrey, 2004; Chen et al., 2013, 2020; Herrmann et

557   al., 2020). Furthermore, inadequate sampling can induce bias (e.g., upscaling from a small

558   number of daytime samples taken during warm-water months can skew apparent patterns;

559   Laruelle et al., 2017; Van Dam et al., 2019.) Using 1 minute sampling intervals, averaged to the

560   hour, reveals patterns in the Rhode River that might otherwise be overlooked. We document the

561   Rhode River as having strong seasonality in both pCO_2 content as well as the extent and

562   direction of CO_2 flux (Figs. 2, S1, S2). Both measures are marked by daily oscillations,

563   frequently reversing direction during a single 24 hr period in warm-water months (Figs. 2) but

564   more stable and unidirectional during cold-water months (Figs. 2 and 5).

565

566   3.8 Shifting Net Ecosystem Production

567   To better understand how the net ecosystem production (NEP) of the Rhode River shifts

568   throughout the year, where positive NEP indicates the river is storing carbon (autotrophic state)

569   and negative NEP indicates it is releasing carbon to the atmosphere (heterotrophic state), we

570   calculated hourly CO_2 flux values, averaged them by day (i.e. 24 hr period) and plotted each in

571   relation to the $\Delta C = 0$ reference. Each day of the 3 yr study was categorized as either net

572   heterotrophic (CO_2 flux from water to atmosphere) or net autotrophic (CO_2 flux from atmosphere

573   to water). Each day was then further identified as either purely heterotrophic (all 24 hours were

574   heterotrophic), purely autotrophic, or mixed (some hours were heterotrophic and some were

575   autotrophic but resulting in a net autotrophic or net heterotrophic state for the day) (Fig. 5). From

576   July 2018 to July 2021, most 24 hr periods were categorized as pure autotrophic (444/920 =

577   48%), while 25% (229/990) were purely heterotrophic, and the remainder of mixed trophic status

578   (17% net heterotrophic and 10% net autotrophic; Fig. 5).

579

580

581
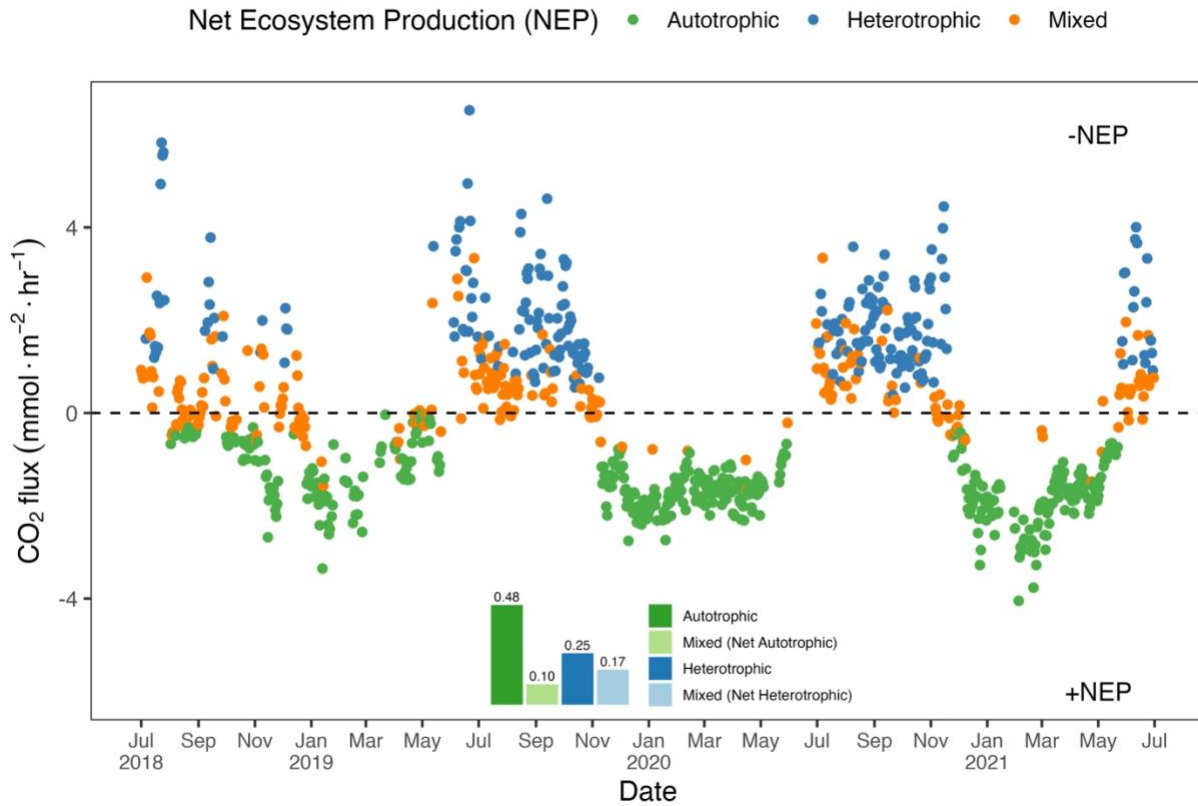
Fig. 5. Daily mean CO_2 flux estimates (CO_2 gradient is $CO_{2water} - CO_{2air}$). Green dots indicate days when all 24 hourly flux measurements were negative (autotrophic with +NEP); blue dots indicate days on which all 24 hourly flux measurements were positive (heterotrophic with -NEP). Orange dots indicate that hourly fluxes were both negative and positive, and the position of the orange dot below or above the zero line indicates whether the day was net autotrophic or net heterotrophic. Insert describes the proportion of days in each category indicating that during 58% (0.48 + 0.10) of days across three years of observation, the Rhode River was a CO_2 sink.

589

Altogether, the Rhode River was net autotrophic for (535 of 920 days = 58%) and net

heterotrophic for 42% (385 days) across three years. When CO_2 flux is integrated over all three

years, the Rhode River is shown to have near neutral NEP (Fig. 6). The effect size of season is

two orders of magnitude greater than either that of day/night or season:day/night interaction

(Table 2). Mean CO_2 flux values highlight the obvious correlation between season and NEP;

error bars (± 1 SD) reveal the importance of diel cycling where the magnitude and directionality

of day/night flux variability is approximately equal to the overall variability accrued across all

three years (Fig. 6). Although CO_2 flux is less variable and more autotrophic during cold-water

598   months than warm-months in the Rhode River, the range of possible values that occur across

599   night and day, regardless of season, must be taken into consideration to minimize incidental

600   sampling bias (Figs. 2 and 6).

601

602   A multi-year investigation of CO_2 flux in the main stem of Chesapeake Bay by Chen et al.

603   (2020) combined several bay-wide cruises that were distributed across seasons to collect discrete

604   and underway pCO_2 data for CO_2 flux calculations. They concluded that the low salinity upper

605   bay, which receives large volumes of freshwater from the Susquehanna River, was net

606   heterotrophic; the mesohaline middle bay was net autotrophic, and the polyhaline lower bay was

607   near carbon neutral. Chen et al. (2020) characterized Chesapeake Bay, on the whole, as a weak

608   source of CO_2 to the atmosphere (net flux = 0.73 mol $\cdot$ m^{-2} $\cdot$ yr^{-1}) but suggested that during wet

609   years, it may function as weak sink of CO_2. Herrmann et al. (2020) also concluded that the

610   Chesapeake Bay was a weak source of CO_2 to the atmosphere based on calculated pCO_2 values

611   from long term pH and alkalinity measurements (net flux = 1.2 mol $\cdot$ m^{-2} $\cdot$ yr^{-1}mol). Brodeur and

612   colleagues (2019) examined dissolved inorganic carbon (DIC) and total alkalinity along the

613   mainstem of the Chesapeake Bay across the year in 2016 and concluded that DIC increases from

614   north to south and from surface waters to depth, but that seasonal riverine input and biological

615   cycling were significantly important, concluding that the Bay as a whole was a sink for CO_2.

616

617   When our annual mean pCO_2 values were compared with the Chen et al. (2020) survey, the

618   Rhode River was shown to be higher on average and more variable than the mesohaline main

619   stem of the Bay (591 $\pm$ 652 vs. 416 $\pm$ 167 µatm), including a substantially greater measured

620   range (min = 15, max = 5182 µatm vs. 103 and 1033 µatm). These results suggest that water in

621   the shallow and well mixed Rhode River, and DIC in particular, undergo more acute biological

622   transformation than in the mesohaline main stem of Chesapeake Bay. Chen et al. (2020) point to

623   a variety of factors that affect pCO_2 and CO_2 flux in the main stem bay, including temperature,

624   depth, stratification, and freshwater input volume, some of which may attenuate biological

625   forcing. Interannual variability was demonstrated in both the Rhode River (some years were net

626   autotrophic and others heterotrophic, Figs. 4 and 5) and in the mesohaline main stem of the Bay;

627   however, we attribute interannual variability in pCO_2 and CO_2 flux primarily to variation in

628   water temperature that in turn drives biological activity. We conclude that seasonal variations the

629   Rhode River (and likely similar rivers in the mesohaline portion of the Chesapeake) are

630   significant and predictable, closely associated with water temperature, and that temperature

631   mediates NEP biologically rather than by changes to the solubility of CO_2.
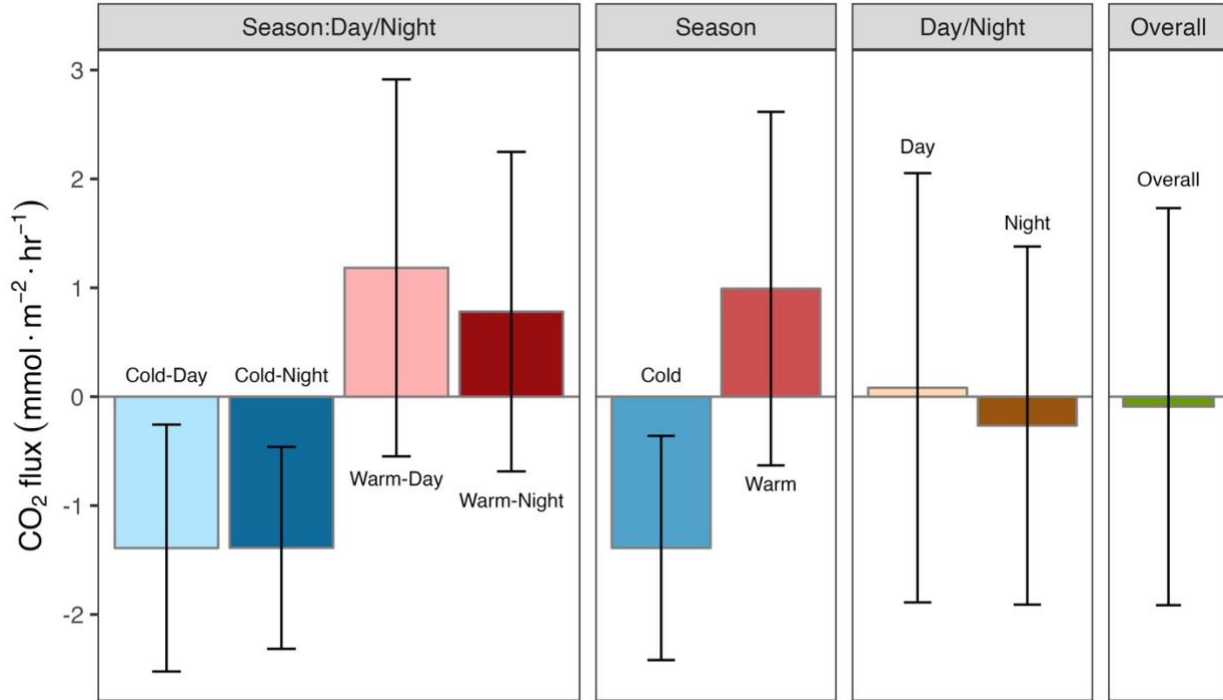
632

633

634   **Fig. 6.** Mean CO_2 flux $\pm$ 1 SD (mmol $\cdot$ m^{-2} $\cdot$ hr^{-1}) plotted by day/night cycling, cold-water/warm-
635   water season, season by day/night interaction, and overall CO_2 flux across three years of
636   observation.

637

638   In the Rhode River, we find that CO_2 flux reverses itself daily for part of the year (June–

639   November) yielding some days that are characterized as a net sink (net autotrophic) and others

640   that are a net source (net heterotrophic). From December to May, diel cycling is minimal and the

641   river is almost exclusively a net sink, autotrophic both day and night. Finally, although CO_2 flux

642   is pronounced but variable across seasons, the net CO_2 flux of the Rhode River on an annual

643   basis is near neutral.

644

645

646

647   3.9 Lateral transport

648   Tidal cycling has been shown to liberate and laterally transport DOC from brackish marshes to

649   adjacent estuaries (Cai, 2011; Herrmann, 2015) and therefore is of great importance to carbon

650   cycling and budgets of wetlands and estuaries (Najjar et al., 2020). DOC outwelling from the

651   Kirkpatrick Marsh (hereafter KPM), a 0.21 km^2 tidal marsh located approximately 1 km up

652   estuary from our primary study site at the SERC Dock (Fig. 1), into the Rhode River has been

653   measured and modeled extensively in recent years (Clark et al., 2020; Menendez et al., 2022;

654   Tzortziou et al., 2011; Tzortziou et al., 2008). These studies indicate that the KPM is responsible

655   for a large portion of overall DOC input to the Rhode River, as well as significant export from

656   the river to the mainstem of Chesapeake Bay. Model generation and validation by Clark et al.

657   (2020) indicate that up to 13.1% of the total DOC input to the Rhode River originates in the

658   KPM. Another important source (53% of total) is DOC derived from phytoplankton and is

659   therefore labile and readily biodegraded and remineralized into DIC. Furthermore, large

660   quantities of other, semi-labile forms of DOC are exported from the KPM, which are themselves

661   subject to photochemical and biodegradation and remineralization (Clark et al., 2020).

662   Importantly, each of these DOC streams provides a potential source of DIC, including pCO$_2$, to

663   the Rhode River.

664

665   Dissolved inorganic carbon generated in brackish tidal wetlands is also outwelled directly into

666   estuaries (e.g., Cai et al., 2000; Chu et al., 2018; Song et al., 2023). Recent work by Song et al.

667   (2023) demonstrates that pCO$_2$ in a salt marsh tidal creek in Waquoit Bay, MA was regulated by

668   both tide height (inversely) and the day/night cycle, with nighttime low tides resulting in the

669   highest pCO$_2$ values, signaling a strong local effect from respiration and photosynthesis in

670   combination with tidal outwelling.

671

672   In the Rhode River watershed pCO$_2$ was measured continuously in the single tidal creek that

673   drains the KPM using the same methods as at our primary study location. We observed that the

674   KPM tidal creek pCO$_2$ follows the tidal cycle exclusively, yet outside the mouth of the tidal

675   creek, in the estuary proper, day/night cycling overwhelms this marsh tidal signal. Simultaneous

676   pCO$_2$ measurements from the SERC dock follow a strict day/night cycle (Fig. S4). However,

677   while peak levels of dissolved CO$_2$ in the Kirkpatrick Marsh creek occur at low tide and can

678   reach values nearly 20 times greater than highs at the SERC dock (Fig. S4) there is no obvious

679   evidence of this tidal DIC input at the dock site. Remineralization of DOC exported from the

680   KPM, as well as DOC originating in other locations within the watershed are important sources

681   of DIC in the river, but given the relative volumes of these sources to that of the much larger

682   estuary, as well as the physical distance (~1 km) from SERC dock, these input signals should be

683   expected to be lagged and damped inside the estuary and not tightly coupled with tidal cycles.

684   Instead, $p\mathrm{CO_2}$ exported from the KPM is expected to undergo significant dilution effects, be

685   partially off-gassed to the atmosphere, and be metabolized via photosynthesis, reducing its

686   influence on downstream sites. These findings suggest that despite periodic extreme $p\mathrm{CO_2}$ in

687   KPM tidal creek (>30,000 ppmv), the overall mass of $\mathrm{CO_2}$ export is not sufficient to have

688   measurable effects on the deeper, well-mixed portions of the Rhode River.

689

690   Thus, although land – sea interfaces and outwelling of DOC and DIC are important in estuaries

691   and coastal ecosystems, the relative sizes of wetlands and adjacent water bodies and the overall

692   volume of water moving between the two are also important factors. In eutrophic estuaries like

693   the Rhode River, biological forcing can rapidly assimilate DIC and degrade and mineralize labile

694   forms of DOC, as evidenced by extensive diel cycling in these systems (e.g., Brodeur et al. 2019;

695   Song et al. 2023, and the present study.) The much larger and complex Chesapeake Bay

696   generally follows seasonal changes in $p\mathrm{CO_2}$ and $\mathrm{CO_2}$ flux, but these appear to be most

697   predictable in the upper oligohaline portion and the polyhaline region of the bay near the mouth,

698   where freshwater and oceanic end-member effects are most pronounced (Brodeur et al. 2019;

699   Chen et al., 2020). The central mesohaline part of Chesapeake Bay comprises numerous discrete

700   and unique watersheds and subestuaries/rivers, each of which exchanges water with the bay.

701   Elucidating spatial and temporal patterns of $p\mathrm{CO_2}$ and $\mathrm{CO_2}$ flux are vital for understanding each

702   one's role as an atmospheric source or sink, but also could provide better insight into how each

703   may be influenced by global increases in atmospheric $\mathrm{CO_2}$ (i.e., acidification and its influences

704   on estuarine metabolism, and the local biota, fisheries, and habitats each support.) Collectively,

705   these and other subestuaries will have cumulative effects on the overall water quality of

706   Chesapeake Bay, including cycling of DOC and DIC, which in turn affect $p\mathrm{CO_2}$ and $\mathrm{CO_2}$ flux.

707

708
709   **4. Conclusion**

710   As indicated in this study and others, the role that biological processes play in estuaries to either

711   fix CO_2 (autotrophy) or liberate CO_2 (heterotrophy) are extensive, complex, and can be quite

712   variable over space and time (Brodeur et al. 2019; Chen et al., 2020; Herrmann et al., 2020;

713   Rosentreter et al., 2021). High frequency automated measurements revealed strong seasonal

714   contrasts in dissolved CO_2 content and CO_2 flux between water and atmosphere of the Rhode

715   River, a shallow mesohaline reach of the Chesapeake Bay. Importantly, only through high

716   frequency, multi-year measurements could diel and seasonal cycling be fully discerned. The

717   timing and frequency of measurements are critical and have potential for strong and misleading

718   biases if sampling is insufficient. In contrast, cold-water months coincide with long periods

719   (weeks to months) of continuous sub-atmospheric sink conditions for CO_2. Using these

720   measurements, we estimated the direction and magnitude of CO_2 flux in hourly, daily, and

721   annual terms. In the Rhode River CO_2 flux reverses itself daily for part of the year (June through

722   November) yielding some days that are characterized as net sink (net autotrophic and NEP > 0)

723   and others that are net source (net heterotrophic and NEP < 0). From December to May diel

724   cycling is minimal, and the river is almost exclusively a CO_2 sink with +NEP both day and night.

725   Although CO_2 flux is pronounced but variable across seasons, the net CO_2 flux of the Rhode

726   River on an annual basis is near carbon neutral, although some years are net heterotrophic and

727   others net autotrophic.

728

729   High frequency sampling of $p$$CO_2$, although typically confined spatially, is one approach to

730   understanding fundamental aspects of estuarine metabolic states and CO_2 flux that may

731   otherwise go undetected (Song et al., 2023). To address the spatial complexity of estuarine,

732   nearshore, and inland waters, more observation locations are required. As with any

733   environmental or ecological question, careful sampling design is critical to balance efficiency

734   and statistical power.

735

736   As the largest and arguably most complex estuary in the United States, the Chesapeake Bay is

737   the subject of extensive ecosystem management efforts and ranks among the most studied and

738   monitored estuaries in the world (Boesch and Goldman 2009). Yet, information on CO_2 and

739   GHG fluxes continue to be limited (Brodeur 2019; Chen et al., 2020; Herrmann et al., 2020).

740   Given the extensive coordinated monitoring programs that either make real-time water quality

741   measurements and/or maintain routine water sampling schedules (e.g., Maryland DNR "Eyes on

742   the Bay" program) in this region, existing water quality observation assets and sampling

743   programs could be leveraged to more fully characterize and quantify CO_2 and other GHG

744   dynamics and flux in the Bay and elsewhere (see Saba et al. 2019). For example, coordinated

745   deployment of additional automated sampling devices (e.g., robust air-water equilibrators and

746   traditional atmospheric gas sensors) in key locations would enable estimates of CO_2 flux, and if

747   combined with pH, DIC, or total alkalinity measurements, carbonate chemistry calculations as

748   well. Importantly, such installations need not be permanent. Instead, a small group of

749   instruments could be systematically deployed across an existing observation network, co-located

750   with other water quality instruments using a stratified sampling approach to capture spatial

751   variability. For example, a set of shifting two to four week deployments during summer and

752   winter months could yield sufficient data to advance our understanding of Chesapeake Bay-wide

753   CO_2 flux significantly in a single year. Such information would complement underway transects

754   that are vital, but which tend to underestimate temporal variability in any given location. In the

755   case of dissolved GHGs, liquid-air equilibration techniques are being used to measure multiple

756   GHGs (Call et al. 2015; Hartmann 2018; Gülzow et al. 2011; Miller et al. 2019; Xiao et al.

757   2020).

758

759   Understanding the GHG dynamics in estuaries is a vital component to generating accurate global

760   budgets (Maher & Eyre, 2012) as well as informing where emerging carbon capture

761   technologies, including nature-based solutions, might be best located (Bradshaw & Dance, 2005;

762   Sun et al., 2021). In the case of estuaries, there have been extensive global losses of seagrasses

763   due to habitat degradation, pollution, and disease (Waycott et al. 2009). In addition to many

764   other ecosystem service benefits, restoration of seagrass and submerged aquatic vegetation has

765   the potential to restore and enhance natural carbon sequestration (i.e. blue carbon; Kennedy et al.

766   2022; Macreadie et al. 2022; Unsworth et al. 2022). In Virginia, U.S.A., Oreska et al. (2020)

767   demonstrated how the functional benefits of a restored seagrass meadow habitat can be

768   quantified ecologically in terms of their ability to sequester carbon and affect GHG fluxes

769   between the estuary and atmosphere. Uniquely, these investigators then monetized the costs and

770   benefits of habitat restoration and function as CO_2 offset credits, as part of a GHG budget, and

771 demonstrated how such approaches can be used to incentivize habitat restoration (Oreska et al.

772 (2020).

773

774 Increasing the completeness and utility of global GHG budgets, as they relate to human activities

775 and ecosystem functions, are necessary steps toward combating global climate change.

776 Measurement of GHGs at high spatial and temporal resolution using economical, automated

777 measurement solutions can increase our understanding of GHG dynamics at small ecologically

778 significant scales, as well as at the larger ecosystem level of an estuary.

779

780 **Data Availability**

781 Hourly means of pCO$_2$ and associated environmental data used in the analyses are available at

782 the Smithsonian Figshare repository https://doi.org/10.25573/serc.22491655 via under Creative

783 Commons license CC BY-NC 4.0.

784

785 **Author Contributions**

786 AWM contributed to project Conceptualization, Funding acquisition, Investigation,

787 Methodology, Project Administration, Resources, Supervision and Writing – Original Draft.

788 JRM contributed to Data Curation, Formal Analysis, Software and Visualization. ACR

789 contributed to Data Curation, Investigation, Methodology and Project Administration. MSM

790 contributed to Conceptualization, Supervision and Visualization. KJK contributed to

791 Conceptualization, Data Curation, Software, Validation. All authors contributed to Writing –

792 review and editing.

793

794 **Competing Interests**

795 The corresponding author has declared that none of the authors has any competing interests.

796

797

798

799

800 **Acknowledgments**

805

806 **References**

807 Abril, G. and Borges, A. V.: Carbon Dioxide and Methane Emissions from Estuaries, in:

808 Greenhouse Gas Emissions — Fluxes and Processes: Hydroelectric Reservoirs and Natural

809 Environments, edited by: Tremblay, A., Varfalvy, L., Roehm, C., and Garneau, M., Springer,

810 Berlin, Heidelberg, 187–207, https://doi.org/10.1007/978-3-540-26643-3_8, 2005.

811 Abril, G., Etcheber, H., Borges, A. V., and Frankignoulle, M.: Excess atmospheric carbon

812 dioxide transported by rivers into the Scheldt estuary, Comptes Rendus de l'Académie des

813 Sciences - Series IIA - Earth and Planetary Science, 330, 761–768,

814 https://doi.org/10.1016/S1251-8050(00)00231-7, 2000.

815 Bauer, J. E., Cai, W.-J., Raymond, P. A., Bianchi, T. S., Hopkinson, C. S., and Regnier, P. A. G.:

816 The changing carbon cycle of the coastal ocean, Nature, 504, 61–70,

817 https://doi.org/10.1038/nature12857, 2013.

818 Benson, S., Rich, R., Tashjian, A., Lonneman, M., and Neale, P.: MarineGEO Upper

819 Chesapeake Bay Observatory CPOP Data, https://doi.org/10.25573/SERC.C.6100368.V10,

820 2023.

821 Boesch, D.F. and Goldman, E.B.: Chesapeake Bay, USA, in: Ecosystem-Based Management for

822 the Oceans, edited by: McLeod, K. McLeod and Leslie H. Island Press, Washington, D.C., 268–

823 293, 2009.

824

825 Borges, A. V.: Do we have enough pieces of the jigsaw to integrate CO2 fluxes in the coastal

826 ocean?, Estuaries, 28, 3–27, https://doi.org/10.1007/BF02732750, 2005.

827   Borges, A. V., Delille, B., Schiettecatte, L.-S., Gazeau, F., Abril, G., and Frankignoulle, M.: Gas

828   transfer velocities of CO2 in three European estuaries (Randers Fjord, Scheldt, and Thames),

829   Limnology and Oceanography, 49, 1630–1641, 2004.

830   Bradshaw, J. and Dance, T.: Mapping geological storage prospectivity of CO2 for the world's

831   sedimentary basins and regional source to sink matching, in: Greenhouse Gas Control

832   Technologies 7, vol. I, Elsevier, 583–591, https://doi.org/10.1016/B978-008044704-9/50059-8,

833   2005.

834   Breitburg, D. L., Hines, A. H., Jordan, T. E., McCormick, M. K., Weller, D. E., and Whigham,

835   D. F.: Landscape patterns, nutrient discharges, and biota of the Rhode River estuary and its

836   watershed: Contribution of the Smithsonian Environmental Research Center to the Pilot

837   Integrated Ecosystem Assessment, 2008.

838   Brodeur, J. R., Chen, B., Su, J., Xu, Y.-Y., Hussain, N., Scaboo, K. M., Zhang, Y., Testa, J. M.,

839   and Cai, W.-J.: Chesapeake Bay Inorganic Carbon: Spatial Distribution and Seasonal Variability,

840   Frontiers in Marine Science, 6, https://doi.org/10.3389/fmars.2019.00099, 2019.

841   Broecker, W. S., Takahashi, T., Simpson, H. J., and Peng, T.-H.: Fate of Fossil Fuel Carbon

842   Dioxide and the Global Carbon Budget, Science, 206, 409–418, 1979.

843   Caffrey, J. M.: Factors controlling net ecosystem metabolism in US estuaries, Estuaries, 27, 90–

844   101, 2004.

845   Cai, W.-J.: Estuarine and Coastal Ocean Carbon Paradox: CO2 Sinks or Sites of Terrestrial

846   Carbon Incineration?, Annual Review of Marine Science, 3, 123–145,

847   https://doi.org/10.1146/annurev-marine-120709-142723, 2011.

848   Cai, W.-J. and Wang, Y.: The chemistry, fluxes, and sources of carbon dioxide in the estuarine

849   waters of the Satilla and Altamaha Rivers, Georgia, Limnology and Oceanography, 43, 657–668,

850   https://doi.org/10.4319/lo.1998.43.4.0657, 1998.

851   Cai, W.-J., Wiebe, W. J., Wang, Y., and Sheldon, J. E.: Intertidal marsh as a source of dissolved

852   inorganic carbon and a sink of nitrate in the Satilla River-estuarine complex in the southeastern

853   U.S., Limnology and Oceanography, 45, 1743–1752, https://doi.org/10.4319/lo.2000.45.8.1743,

854   2000.

855 Call, M., Maher, D. T., Santos, I. R., Ruiz-Halpern, S., Mangion, P., Sanders, C. J., Erler, D. V.,

856 Oakes, J. M., Rosentreter, J., Murray, R., and Eyre, B. D.: Spatial and temporal variability of

857 carbon dioxide and methane fluxes over semi-diurnal and spring–neap–spring timescales in a

858 mangrove creek, Geochimica et Cosmochimica Acta, 150, 211–225,

859 https://doi.org/10.1016/j.gca.2014.11.023, 2015.

860 Chen, B., Cai, W.-J., Brodeur, J. R., Hussain, N., Testa, J. M., Ni, W., and Li, Q.: Seasonal and

861 spatial variability in surface pCO2 and air–water CO2 flux in the Chesapeake Bay, Limnology

862 and Oceanography, 65, 3046–3065, https://doi.org/10.1002/lno.11573, 2020.

863 Chen, C.-T. A., Huang, T.-H., Chen, Y.-C., Bai, Y., He, X., and Kang, Y.: Air–sea exchanges of

864 CO2 in the world's coastal seas, Biogeosciences, 10, 6509–6544, https://doi.org/10.5194/bg-10-

865 6509-2013, 2013.

866 Chu, S. N., Wang, Z. A., Gonneea, M. E., Kroeger, K. D., and Ganju, N. K.: Deciphering the

867 dynamics of inorganic carbon export from intertidal salt marshes using high-frequency

868 measurements, Marine Chemistry, 206, 7–18, https://doi.org/10.1016/j.marchem.2018.08.005,

869 2018.

870 Clark, J. B., Long, W., Tzortziou, M., Neale, P. J., and Hood, R. R.: Wind-Driven Dissolved

871 Organic Matter Dynamics in a Chesapeake Bay Tidal Marsh-Estuary System, Estuaries and

872 Coasts, 41, 708–723, https://doi.org/10.1007/s12237-017-0295-1, 2018.

873 Clark, J. B., Long, W., and Hood, R. R.: A Comprehensive Estuarine Dissolved Organic Carbon

874 Budget Using an Enhanced Biogeochemical Model, Journal of Geophysical Research:

875 Biogeosciences, 125, e2019JG005442, https://doi.org/10.1029/2019JG005442, 2020.

876 Correll, D. L., Jordan, T. E., and Weller, D. E.: Nutrient flux in a landscape: Effects of coastal

877 land use and terrestrial community mosaic on nutrient transport to coastal waters, Estuaries, 15,

878 431–442, https://doi.org/10.2307/1352388, 1992.

879 Dai, M., Su, J., Zhao, Y., Hofmann, E. E., Cao, Z., Cai, W.-J., Gan, J., Lacroix, F., Laruelle, G.

880 G., Meng, F., Müller, J. D., Regnier, P. A. G., Wang, G., and Wang, Z.: Carbon Fluxes in the

881 Coastal Ocean: Synthesis, Boundary Processes, and Future Trends, Annual Review of Earth and

882 Planetary Sciences, 50, 593–626, https://doi.org/10.1146/annurev-earth-032320-090746, 2022.

883 Frankignoulle, M., Abril, G., Borges, A., Bourge, I., Canon, C., Delille, B., Libert, E., and

884 Théate, J.-M.: Carbon Dioxide Emission from European Estuaries, Science, 282, 434–436,

885 https://doi.org/10.1126/science.282.5388.434, 1998.

886 Freeman, L. A., Corbett, D. R., Fitzgerald, A. M., Lemley, D. A., Quigg, A., and Steppe, C. N.:

887 Impacts of urbanization and development on estuarine ecosystems and water quality, Estuaries

888 and Coasts, 42, 1821–1838, https://doi.org/10.1007/s12237-019-00597-z, 2019.

889 Freshwater Flow into Chesapeake Bay | U.S. Geological Survey:

890 https://www.usgs.gov/centers/chesapeake-bay-activities/science/freshwater-flow-chesapeake-

891 bay, last access: 21 September 2023.

892 Gallegos, C. L., Jordan, T. E., and Correll, D. L.: Event-scale response of phytoplankton to

893 watershed inputs in a subestuary: Timing, magnitude, and location of blooms, Limnology and

894 Oceanography, 37, 813–828, https://doi.org/10.4319/lo.1992.37.4.0813, 1992.

895 Gallegos, C. L., Jordan, T. E., and Hedrick, S. S.: Long-term Dynamics of Phytoplankton in the

896 Rhode River, Maryland (USA), Estuaries and Coasts, 33, 471–484,

897 https://doi.org/10.1007/s12237-009-9172-x, 2010.

898 Gattuso, J.-P., Frankignoulle, M., and Wollast, R.: Carbon and Carbonate Metabolism in Coastal

899 Aquatic Ecosystems, Annual Review of Ecology and Systematics, 29, 405–434,

900 https://doi.org/10.1146/annurev.ecolsys.29.1.405, 1998.

901 Gülzow, W., Rehder, G., Schneider, B., Deimling, J. S. v., and Sadkowiak, B.: A new method for

902 continuous measurement of methane and carbon dioxide in surface waters using off-axis

903 integrated cavity output spectroscopy (ICOS): An example from the Baltic Sea, Limnology and

904 Oceanography: Methods, 9, 176–184, https://doi.org/10.4319/lom.2011.9.176, 2011.

905 Hartmann, J. F., Gentz, T., Schiller, A., Greule, M., Grossart, H.-P., Ionescu, D., Keppler, F.,

906 Martinez-Cruz, K., Sepulveda-Jauregui, A., and Isenbeck-Schröter, M.: A fast and sensitive

907 method for the continuous in situ determination of dissolved methane and its δ13C-isotope ratio

908 in surface waters, Limnology and Oceanography: Methods, 16, 273–285,

909 https://doi.org/10.1002/lom3.10244, 2018.

910   Herrmann, M., Najjar, R. G., Kemp, W. M., Alexander, R. B., Boyer, E. W., Cai, W.-J., Griffith,

911   P. C., Kroeger, K. D., McCallister, S. L., and Smith, R. A.: Net ecosystem production and

912   organic carbon balance of U.S. East Coast estuaries: A synthesis approach, Global

913   Biogeochemical Cycles, 29, 96–111, https://doi.org/10.1002/2013GB004736, 2015.

914   Herrmann, M., Najjar, R. G., Da, F., Friedman, J. R., Friedrichs, M. A. M., Goldberger, S.,

915   Menendez, A., Shadwick, E. H., Stets, E. G., and St-Laurent, P.: Challenges in Quantifying Air-

916   Water Carbon Dioxide Flux Using Estuarine Water Quality Data: Case Study for Chesapeake

917   Bay, Journal of Geophysical Research: Oceans, 125, e2019JC015610,

918   https://doi.org/10.1029/2019JC015610, 2020.

919   Ho, D. T., Coffineau, N., Hickman, B., Chow, N., Koffman, T., and Schlosser, P.: Influence of

920   current velocity and wind speed on air-water gas exchange in a mangrove estuary, Geophysical

921   Research Letters, 43, 3813–3821, https://doi.org/10.1002/2016GL068727, 2016.

922   Jiang, L.-Q., Cai, W.-J., and Wang, Y.: A comparative study of carbon dioxide degassing in

923   river-and marine-dominated estuaries, Limnology and Oceanography, 53, 2603–2615, 2008.

924   Joesoef, A., Huang, W.-J., Gao, Y., and Cai, W.-J.: Air–water fluxes and sources of carbon

925   dioxide in the Delaware Estuary: spatial and seasonal variability, Biogeosciences, 12, 6085–

926   6101, https://doi.org/10.5194/bg-12-6085-2015, 2015.

927   Jordan, T. E. and Correll, D. L.: Continuous automated sampling of tidal exchanges of nutrients

928   by brackish marshes, Estuarine, Coastal and Shelf Science, 32, 527–545,

929   https://doi.org/10.1016/0272-7714(91)90073-K, 1991.

930   Jordan, T. E., Correll, D. L., Peterjohn, W. T., and Weller, D. E.: Nutrient flux in a landscape:

931   The Rhode River watershed and receiving waters, in: Watershed Research Perspectives, edited

932   by: Correll, D. L., Smithsonian Institution Press, Washington, DC, 1986.

933   Jordan, T. E., Correll, D. L., Miklas, J., and Weller, D. E.: Nutrients and chlorophyll at the

934   interface of a watershed and an estuary, Limnol. Oceanogr., 36, 251–267,

935   https://doi.org/10.4319/lo.1991.36.2.0251, 1991.

936   Kennedy, H., Pagès, J. F., Lagomasino, D., Arias-Ortiz, A., Colarusso, P., Fourqurean, J. W.,

937   Githaiga, M. N., Howard, J. L., Krause-Jensen, D., Kuwae, T., Lavery, P. S., Macreadie, P. I.,

938   Marbà, N., Masqué, P., Mazarrasa, I., Miyajima, T., Serrano, O., and Duarte, C. M.: Species

939   Traits and Geomorphic Setting as Drivers of Global Soil Carbon Stocks in Seagrass Meadows,

940   Global Biogeochemical Cycles, 36, e2022GB007481, https://doi.org/10.1029/2022GB007481,

941   2022.

942   Klaus, M. and Vachon, D.: Challenges of predicting gas transfer velocity from wind

943   measurements over global lakes, Aquat Sci, 82, 53, https://doi.org/10.1007/s00027-020-00729-9,

944   2020.

945   Lachin, J. M.: Fallacies of last observation carried forward analyses, Clinical Trials, 13, 161–

946   168, https://doi.org/10.1177/1740774515602688, 2016.

947   Laruelle, G. G., Goossens, N., Arndt, S., Cai, W.-J., and Regnier, P.: Air–water CO_2 evasion

948   from US East Coast estuaries, Biogeosciences, 14, 2441–2468, https://doi.org/10.5194/bg-14-

949   2441-2017, 2017.

950   Macreadie, P. I., Robertson, A. I., Spinks, B., Adams, M. P., Atchison, J. M., Bell-James, J.,

951   Bryan, B. A., Chu, L., Filbee-Dexter, K., Drake, L., Duarte, C. M., Friess, D. A., Gonzalez, F.,

952   Grafton, R. Q., Helmstedt, K. J., Kaebernick, M., Kelleway, J., Kendrick, G. A., Kennedy, H.,

953   Lovelock, C. E., Megonigal, J. P., Maher, D. T., Pidgeon, E., Rogers, A. A., Sturgiss, R.,

954   Trevathan-Tackett, S. M., Wartman, M., Wilson, K. A., and Rogers, K.: Operationalizing

955   marketable blue carbon, One Earth, 5, 485–492, https://doi.org/10.1016/j.oneear.2022.04.005,

956   2022.

957   Maher, D. T. and Eyre, B. D.: Carbon budgets for three autotrophic Australian estuaries:

958   Implications for global estimates of the coastal air-water CO2 flux, Global Biogeochemical

959   Cycles, 26, https://doi.org/10.1029/2011GB004075, 2012.

960   Martin, C. R., Zeng, N., Karion, A., Dickerson, R. R., Ren, X., Turpie, B. N., and Weber, K. J.:

961   Evaluation and environmental correction of ambient CO_2 measurements from a low-cost NDIR

962   sensor, Atmospheric Measurement Techniques, 10, 2383–2395, https://doi.org/10.5194/amt-10-

963   2383-2017, 2017.

964   Menendez, A., Tzortziou, M., Neale, P., Megonigal, P., Powers, L., Schmitt-Kopplin, P., and

965   Gonsior, M.: Strong Dynamics in Tidal Marsh DOC Export in Response to Natural Cycles and

966 Episodic Events From Continuous Monitoring, Journal of Geophysical Research:

967 Biogeosciences, 127, e2022JG006863, https://doi.org/10.1029/2022JG006863, 2022.

968 Miller, A. W., Reynolds, A. C., and Minton, M. S.: A spherical falling film gas-liquid

969 equilibrator for rapid and continuous measurements of CO2 and other trace gases, PLOS ONE,

970 14, e0222303, https://doi.org/10.1371/journal.pone.0222303, 2019.

971 Najjar, R. G., Herrmann, M., Cintrón Del Valle, S. M., Friedman, J. R., Friedrichs, M. A. M.,

972 Harris, L. A., Shadwick, E. H., Stets, E. G., and Woodland, R. J.: Alkalinity in Tidal Tributaries

973 of the Chesapeake Bay, Journal of Geophysical Research: Oceans, 125, e2019JC015597,

974 https://doi.org/10.1029/2019JC015597, 2020.

975 Oreska, M. P. J., McGlathery, K. J., Aoki, L. R., Berger, A. C., Berg, P., and Mullins, L.: The

976 greenhouse gas offset potential from seagrass restoration, Sci Rep, 10, 7325,

977 https://doi.org/10.1038/s41598-020-64094-1, 2020.

978 Raymond, P. A. and Cole, J. J.: Gas Exchange in Rivers and Estuaries: Choosing a Gas Transfer

979 Velocity, Estuaries, 24, 312–317, https://doi.org/10.2307/1352954, 2001.

980 Raymond, P. A., Hartmann, J., Lauerwald, R., Sobek, S., McDonald, C., Hoover, M., Butman,

981 D., Striegl, R., Mayorga, E., Humborg, C., Kortelainen, P., Dürr, H., Meybeck, M., Ciais, P., and

982 Guth, P.: Global carbon dioxide emissions from inland waters, Nature, 503, 355–359,

983 https://doi.org/10.1038/nature12760, 2013.

984 Rose, K. C., Neale, P. J., Tzortziou, M., Gallegos, C. L., and Jordan, T. E.: Patterns of spectral,

985 spatial, and long-term variability in light attenuation in an optically complex sub-estuary,

986 Limnology and Oceanography, 64, S257–S272, https://doi.org/10.1002/lno.11005, 2019.

987 Rosentreter, J. A., Wells, N. S., Ulseth, A. J., and Eyre, B. D.: Divergent Gas Transfer Velocities

988 of CO2, CH4, and N2O Over Spatial and Temporal Gradients in a Subtropical Estuary, Journal

989 of Geophysical Research: Biogeosciences, 126, e2021JG006270,

990 https://doi.org/10.1029/2021JG006270, 2021.

991 Saba, G. K., Goldsmith, K. A., Cooley, S. R., Grosse, D., Meseck, S. L., Miller, A. W., Phelan,

992 B., Poach, M., Rheault, R., St.Laurent, K., Testa, J. M., Weis, J. S., and Zimmerman, R.:

993 Recommended priorities for research on ecological impacts of ocean and coastal acidification in

994   the U.S. Mid-Atlantic, Estuarine, Coastal and Shelf Science, 225, 106188,

995   https://doi.org/10.1016/j.ecss.2019.04.022, 2019.

996   Saucier, W. J.: Principles of Meteorological Analysis, Dover Publications, 468 pp., 2003.

997   Song, S., Wang, Z. A., Kroeger, K. D., Eagle, M., Chu, S. N., and Ge, J.: High-frequency

998   variability of carbon dioxide fluxes in tidal water over a temperate salt marsh, Limnology and

999   Oceanography, 68, 2108–2125, https://doi.org/10.1002/lno.12409, 2023.

1000   Spada, S., Quartagno, M., Tamburini, M., and Robinson, D.: orcutt: Estimate Procedure in Case

1001   of First Order Autocorrelation, 2018.

1002   Sun, X., Alcalde, J., Bakhtbidar, M., Elío, J., Vilarrasa, V., Canal, J., Ballesteros, J., Heinemann,

1003   N., Haszeldine, S., Cavanagh, A., Vega-Maza, D., Rubiera, F., Martínez-Orio, R., Johnson, G.,

1004   Carbonell, R., Marzan, I., Travé, A., and Gomez-Rivas, E.: Hubs and clusters approach to unlock

1005   the development of carbon capture and storage – Case study in Spain, Applied Energy, 300,

1006   117418, https://doi.org/10.1016/j.apenergy.2021.117418, 2021.

1007   Susquehanna River at Conowingo, MD | U.S. Geological Survey:

1008   https://waterdata.usgs.gov/monitoring-location/01578310/, last access: 28 September 2023.

1009   Takahashi, T., Sutherland, S. C., Sweeney, C., Poisson, A., Metzl, N., Tilbrook, B., Bates, N.,

1010   Wanninkhof, R., Feely, R. A., Sabine, C., Olafsson, J., and Nojiri, Y.: Global sea–air CO2 flux

1011   based on climatological surface ocean pCO2, and seasonal biological and temperature effects,

1012   Deep Sea Research Part II: Topical Studies in Oceanography, 49, 1601–1622,

1013   https://doi.org/10.1016/S0967-0645(02)00003-6, 2002.

1014   Thoning, K. W., Crotwell, A. M., and Mund, J. W.: NOAA Global Monitoring Laboratory

1015   Carbon Cycle and Greenhouse Gases Group Continuous Insitu Measurements of CO2 at Global

1016   Background Sites, 1973-Present, https://doi.org/10.15138/YAF1-BK21, 2023.

1017   Tzortziou, M., Neale, P. J., Osburn, C. L., Megonigal, J. P., Maie, N., and JaffÉ, R.: Tidal

1018   marshes as a source of optically and chemically distinctive colored dissolved organic matter in

1019   the Chesapeake Bay, Limnology and Oceanography, 53, 148–159,

1020   https://doi.org/10.4319/lo.2008.53.1.0148, 2008.

Tzortziou, M., Neale, P. J., Megonigal, J. P., Pow, C. L., and Butterworth, M.: Spatial gradients in dissolved carbon due to tidal marsh outwelling into a Chesapeake Bay estuary, Marine Ecology Progress Series, 426, 41–56, https://doi.org/10.3354/meps09017, 2011.

Unsworth, R. K. F., Cullen-Unsworth, L. C., Jones, B. L. H., and Lilley, R. J.: The planetary role of seagrass conservation, Science, 377, 609–613, https://doi.org/10.1126/science.abq6923, 2022.

Upstill-Goddard, R. C.: Air–sea gas exchange in the coastal zone, Estuarine, Coastal and Shelf Science, 70, 388–404, https://doi.org/10.1016/j.ecss.2006.05.043, 2006.

Van Dam, B. R., Edson, J. B., and Tobias, C.: Parameterizing Air-Water Gas Exchange in the Shallow, Microtidal New River Estuary, Journal of Geophysical Research: Biogeosciences, 124, 2351–2363, https://doi.org/10.1029/2018JG004908, 2019.

Wanninkhof, R.: Relationship between wind speed and gas exchange over the ocean, Journal of Geophysical Research: Oceans, 97, 7373–7382, 1992.

Wanninkhof, R.: Relationship between wind speed and gas exchange over the ocean revisited, Limnology and Oceanography: Methods, 12, 351–362, https://doi.org/10.4319/lom.2014.12.351, 2014.

Wanninkhof, R. and McGillis, W. R.: A cubic relationship between air-sea CO2 exchange and wind speed, Geophysical Research Letters, 26, 1889–1892, https://doi.org/10.1029/1999GL900363, 1999.

Wanninkhof, R., Park, G.-H., Takahashi, T., Sweeney, C., Feely, R., Nojiri, Y., Gruber, N., Doney, S. C., McKinley, G. A., Lenton, A., Le Quéré, C., Heinze, C., Schwinger, J., Graven, H., and Khatiwala, S.: Global ocean carbon uptake: magnitude, variability and trends, Biogeosciences, 10, 1983–2000, https://doi.org/10.5194/bg-10-1983-2013, 2013.

Waycott, M., Duarte, C. M., Carruthers, T. J. B., Orth, R. J., Dennison, W. C., Olyarnik, S., Calladine, A., Fourqurean, J. W., Heck, K. L., Hughes, A. R., Kendrick, G. A., Kenworthy, W. J., Short, F. T., and Williams, S. L.: Accelerating loss of seagrasses across the globe threatens coastal ecosystems, Proceedings of the National Academy of Sciences, 106, 12377–12381, https://doi.org/10.1073/pnas.0905620106, 2009.

1048   Weiss, R. and Price, B.: Nitrous oxide solubility in water and seawater, Marine Chemistry, 8,

1049   347–359, https://doi.org/10.1016/0304-4203(80)90024-9, 1980.

1050   Winslow, L. A., Zwart, J. A., Batt, R. D., Dugan, H. A., Woolway, R. I., Corman, J. R., and

1051   Read, J. S.: LakeMetabolizer: An R package for estimating lake metabolism from free-water

1052   oxygen using diverse statistical models, Inland Waters, 6, https://doi.org/10.1080/IW-6.4.883,

1053   2016.

1054   Xiao, S., Liu, L., Wang, W., Lorke, A., Woodhouse, J., and Grossart, H.-P.: A Fast-Response

1055   Automated Gas Equilibrator (FaRAGE) for continuous in situ measurement of CH_4 and CO_2

1056   dissolved in water, Hydrology and Earth System Sciences, 24, 3871–3880,

1057   https://doi.org/10.5194/hess-24-3871-2020, 2020.

1058   Zeebe, R. E. and Wolf-Gladrow, D.: CO2 in Seawater: Equilibrium, Kinetics, Isotopes, Gulf

1059   Professional Publishing, 382 pp., 2001.

1060

1061 **Supplemental**
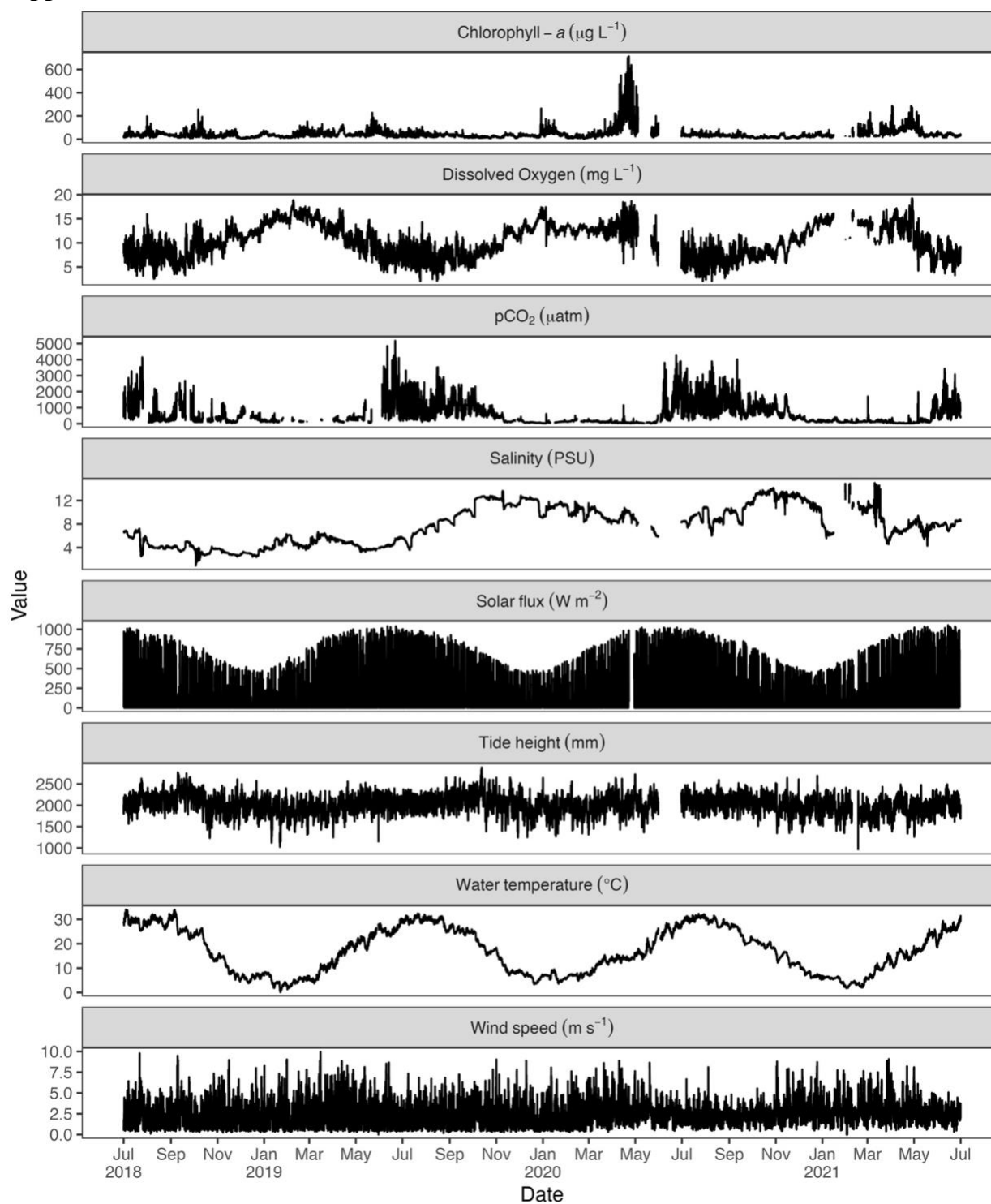
1062
1063 **Fig. S1**. Plot of all raw values from environmental variables for the same time period as CO_2 flux
1064 (July 2018–July 2021).
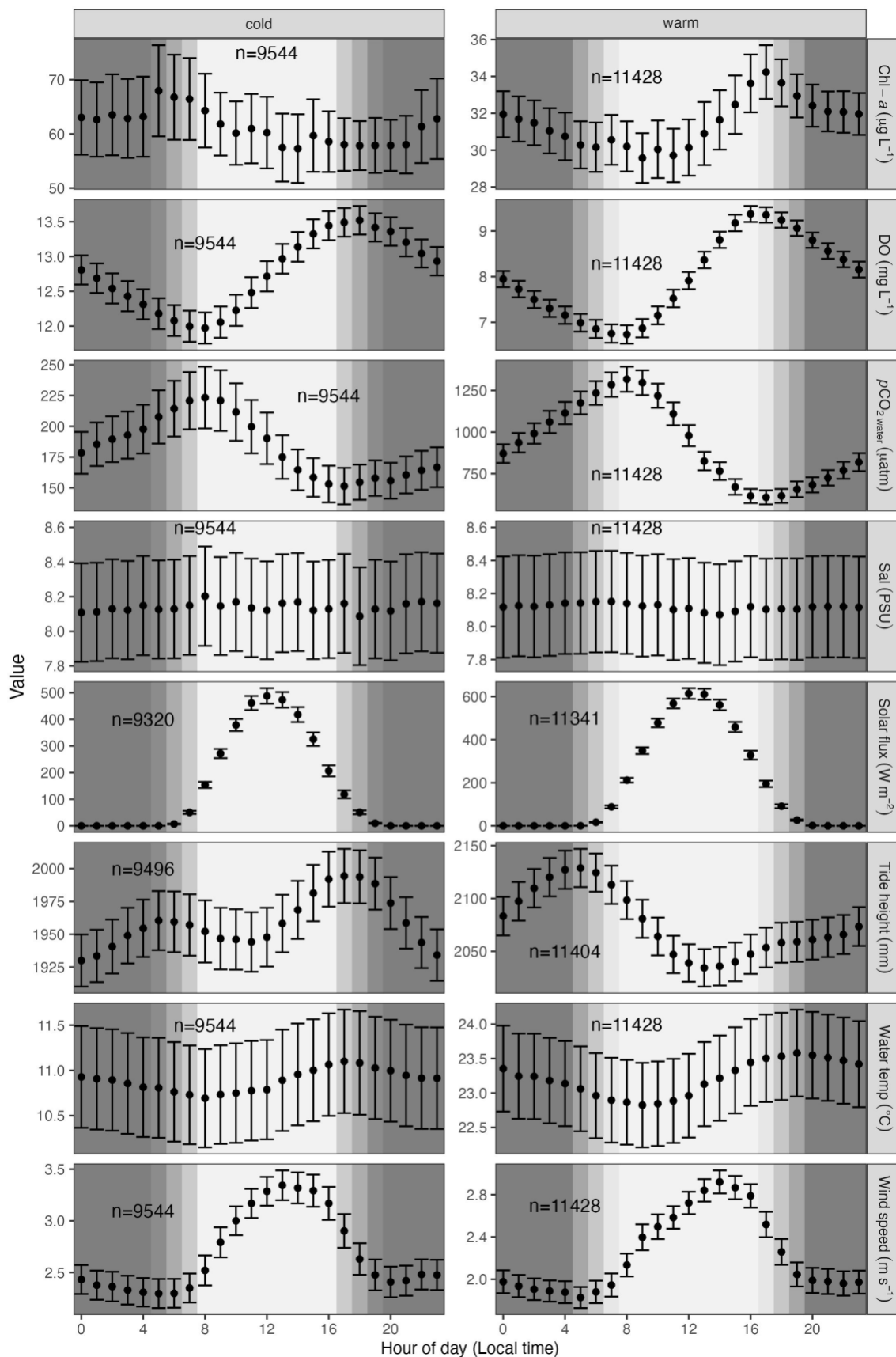
1066   **Fig. S2**. Average hourly values (95% CI) of environmental variables across 24 hours of the day
1067   (July 2018–July 2021) in cold and warm seasons. Light/dark background indicates day/night
1068   conditions.
1069
1070
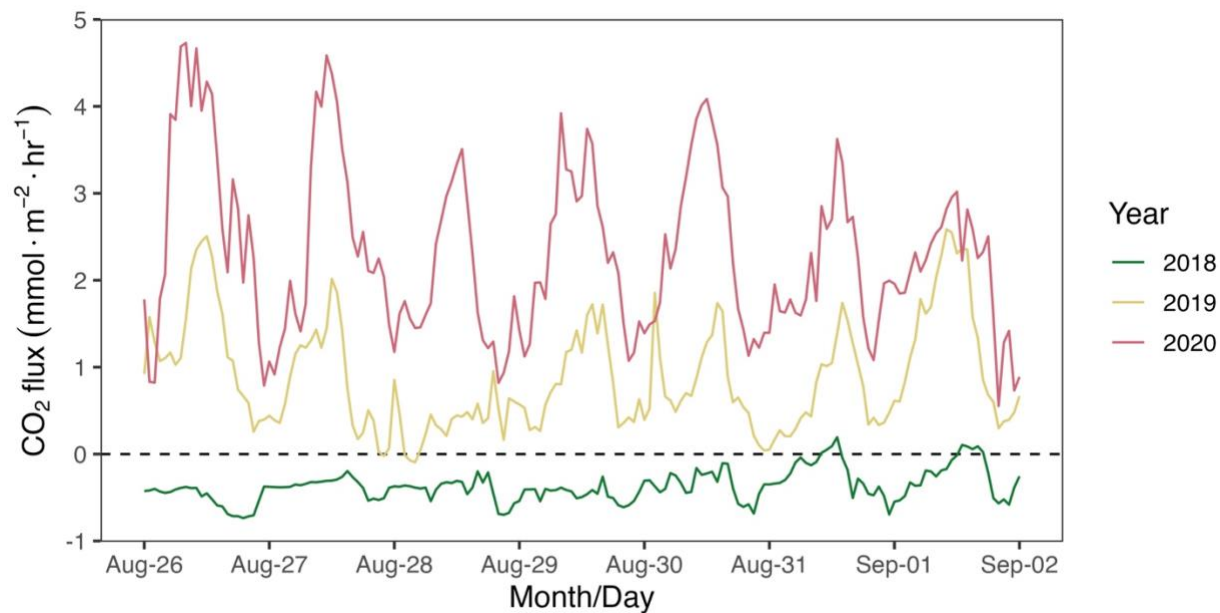
1071
1072   **Fig. S3.** Hourly CO_2 flux estimates for the week of August 26 to September 2 where CO_2 flux
1073   status differs among years.
1074
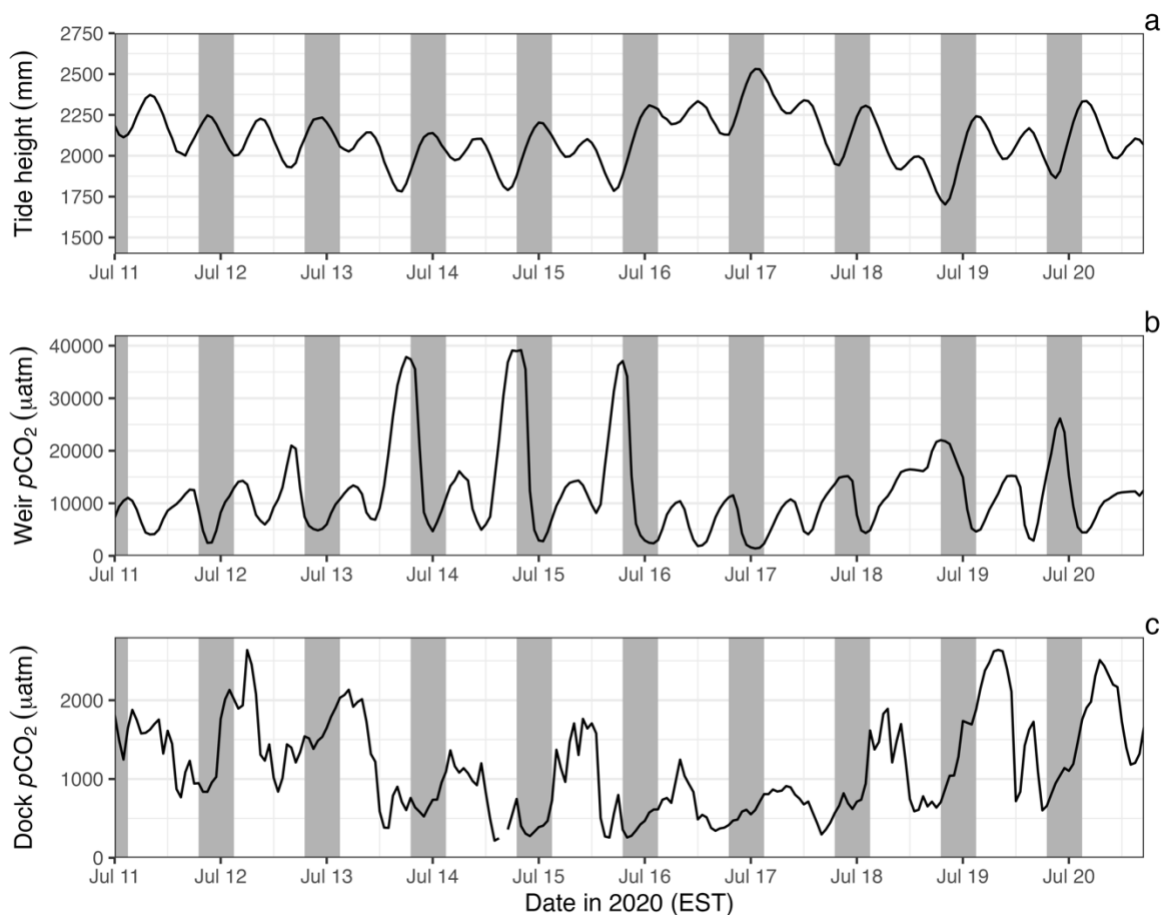
1075
1076 **Fig. S4.** Simultaneous pCO$_2$ measurements (1 hr intervals) from SERC dock (panel c) and the
1077 mouth of the single tidal creek that drains the Kirkpatrick Marsh (panel b) (11–20 Jul 2020)
1078 indicate that dissolved CO$_2$ varies at the dock according to a day/night cycle while CO$_2$ in the
1079 marsh tidal creek rises and falls inversely with tide height (panel a), indicating outwelling of
1080 marsh derived CO$_2$ (e.g., root respiration, pore and groundwater).